# MICROMAGNETIC ANALYSIS OF MAGNETIC NANOPARTICLES FOR HYPERTHERMIA CANCER TREATMENT AND OF TRANSITION CHARACTERISTICS FOR RECORDING MEDIA

A DISSERTATION
SUBMITTED TO THE FACULTY OF THE GRADUATE SCHOOL
OF THE UNIVERSITY OF MINNESOTA
BY

HWEERIN SOHN

IN PARTIAL FULFILLMENT OF THE REQUIREMENTS
FOR THE DEGREE OF
DOCTOR OF PHILOSOPHY

RANDALL H. VICTORA, ADVISOR

OCTOBER, 2012

# Acknowledgements

I acknowledge the helps and contributions from many people during my Ph.D at the University of Minnesota. First of all, I sincerely appreciate the invaluable guidance, education, and support from my advisor, Professor Randall H. Victora. He initiated me into the world of magnetic material research and kindly guided me to learn micromagnetic theory and physical principles. He is also a great teacher in setting up an optimistic attitude toward life. It is my great pleasure to work with him and it is a wonderful experience being his student. I would also like to acknowledge the advice and their valuable comments on my research from Professor Jian-ping Wang, Professor Beth Stadler and Professor Jack Judy during my research work.

Also I give my sincere thanks to my Ph.D committee for their good suggestion and sincere help for my research: Professor Jian-Ping Wang, Professor Beth Stadler, and Professor Timothy Wiedmann.

There are many other people that cheered and helped me. Especially, I sincerely appreciate the help and contributions of The Center for Micromagnetics and Information Technologies (MINT) group members, that is, Xi Chen, Stephanie Hernandez, Yan Dong, Eunkyung Cho, Tao Qu, Pin-wei Huang, Sean Morgan, Yao Wang, Yisong Zhang, Nian Ji, Liang Tu, Ying Jing, Todd Klein, Yuanpeng Li and many other friends for their valuable discussion. I enjoyed the time with them.

Also, I thank the University of Minnesota Supercomputing Institute for computer time and the Medical Device Center of Institute of Engineering in

Medicine at University of Minnesota and National Science Foundation BME 0730825 and Seagate Technology for financial support.

Finally, I would like to thank my family and my fiancé for their support throughout this work. Especially I would like to give my sincere thanks to my parents and my brother for their love, support and encouragement.

# Dedication

With love and gratitude to my parents.

# Abstract

Research has recently focused on magnetic nanoparticles due to fascinating properties that could see great potential employment in biomedicine as well as data storage devices. Micromagnetic analysis was utilized in order to predict the dynamic motion for the magnetization vector of magnetic nanoparticles in biomedical application (hyperthermia cancer therapy) and magnetic information storage (hard disk drive). In this dissertation, the heating properties of magnetic nanoparticles for hyperthermia and the characteristics of magnetic recording media (both conventional perpendicular media and exchange coupled composite media) with a soft underlayer and an antiferromagnetic soft underlayer are presented.

Magnetic nanoparticles have great potential as heating elements for use in hyperthermia. One of the critical issues with widely used iron-oxide compounds such as magnetite and mag-hematite nanoparticles is the relatively low magnetic moment, which results in low heating efficiency. To overcome this demerit, nonoxide high moment $Fe_{70}Co_{30}$ nanoparticles were considered. The mean size of particles was 12nm with 13.6% standard deviation. Micromagnetic simulation of particles' experimental hysteresis loop suggests that their behavior is dominated by a uniaxial anisotropy.

In order to understand the source of energy loss in hyperthermia, magnetic anisotropy and applied field have been optimized for iron cobalt nanocrystalline particles using numerical micromagnetics. The optimized anisotropy energy is 7.6 $k_BT$ at 500 kHz and the hysteresis loss at this optimized energy is approximately $120\times10^6$ ergs/s/g for a very small oscillating field of magnitude 10 Oe. We have also investigated the effects of varying the applied field and find that the addition of a 20 Oe static field applied perpendicular to the oscillating field approximately doubles the energy loss without subjecting the patient to additional radiation. This is an important benefit for magnetic hyperthermia.

To achieve higher areal density in magnetic recording media, the general method is to reduce and make more uniform the grain size, while augmenting the media anisotropy in order to maintain stability. Transition jitter and shape have been studied for “soft” exchange coupled composite (ECC) media and conventional perpendicular media at equal grain size using micromagnetic simulation. A realistic medium having nonuniform grain size has been employed. Media anisotropies are optimized to reduce the high density jitter for ECC and conventional media. Surprisingly, jitter is slightly decreased at high temperature for both media types. Eye diagrams show that short bit length amplitude is higher for ECC by approximately 10 % at room temperature. This indicates that sharper transitions were obtained for ECC media particularly at 300 K where the thermal stability of ECC media presumably aids the write process.

A key component of perpendicular recording has long been the soft underlayer. Conventional perpendicular media and “soft” exchange coupled composite (ECC) media with a conventional soft underlayer (SUL) and an antiferromagnetic soft underlayer (AF-SUL) have been investigated using micromagnetic simulation. The fast Fourier transform (FFT) technique and graphics processing unit (GPU) based computing have been used to reduce the intensive computation time for magnetostatic interactions between the head, SUL, and recording layer. Interestingly, the jitter is always less dependent on reader offset from track center with the AF-SUL. Jitter for ECC media is also shown to depend less strongly on reader offset than for conventional media. The transition center deviation at the optimal anisotropy for both recording layers is lower with the AF-SUL at both linear densities considered. We further find that the track center moves alternately with direction of fringing field as expected from magnetostatic considerations.

## Table of Contents

## List of Figures

# Chapter 1 Introduction

## 1.1 Fundamental magnetism

### 1.1.1 History of magnetism

The early use of magnetism is found in most of the world civilizations. The most popular legend for the discovery of magnets is found in a book of Chinese history, or by Greeks about 4,000 years ago [1.1], [1.2], [1.3]. Permanent magnets are widespread in nature in the form of lodestones which consist of pure or nearly pure magnetite, the iron oxide $Fe_3O_4$. For a few centuries, the lodestone was used to point in a north-south direction creating a primitive compass, despite a lack of scientific understanding knowledge. French scholar Peter Peregrinus of Maricourt conducted experiments on magnetism and described the properties of magnets in the $13^{th}$ century [1.4]. However, much significant progress was made with the experiments of William Gilbert in 1600. His monograph De Magnete was the first modern scientific text to explain that the Earth was a giant magnet and that the direction of the dipole field was examined at the surface of a lodestone sphere [1.5]. Magnetic research progressed rapidly after Hans-Christian Oersted discovered the truth that a current-carrying wire produced a circumferential magnetic field affecting the direction of a compass needle in 1820. In the same period, French mathematician and physicist, Andre-Ampere Marie also showed that a current-carrying wound wire was equivalent to a magnet and this is well known as Ampere's circuital law [1.5]. In series of the remarkable discoveries, Jean-Baptiste Biot and Felix Savart came up with the Biot-Savart Law which gives the formalism

for the magnetic field from a current carrying wire and Michael Faraday discovered electromagnetic induction and diamagnetism. All these experimental works motivated James Clerk Maxwell who established the unified theory of the inter-relationships between electricity and magnetism in 1864. Despite the technical and academic improvements of the understanding of electromagnetic phenomena, the principle behind ferromagnetic solid materials remained in question.

### 1.1.2 Origin of magnetic moments

In order to comprehend the unique properties of various kinds of magnetic materials, one should first understand the fundamental concept of a magnetic moment. The magnetic moment of a magnet is a vectorial quantity that determines the magnetic force that the magnet exerts on an electric current and also the torque that a magnetic field exerts on it. A magnet produces a magnetic field having a magnitude and direction. This magnetic field is proportional to the magnetic moment. For some objects, this magnetic moment implies a magnetic dipole moment. For instance, a bar magnet having magnetic poles of equal strength "$p$" at each end and length "$l$" illustrates the magnetic moments in materials. When the bar magnet is located in a magnetic field, it will be affected by the field and tend to align to the same direction as the field. This torque is magnetic moment and it is defined as

$$m = pl, \tag{1.1}$$

where $m$ is the magnetic moment of the magnet [1.6]. If the bar magnet in a magnetic field is not aligned with the field direction, a certain amount of potential energy relative to the parallel position will be generated. The unit of potential

energy is in ergs, and the unit of magnetic moment, $m$ is erg/Oe, or simply the electromagnetic unit of magnetic moment (*emu*). Equation 1.1 implies that the total magnetic moment is equal to the sum of the magnetic moments of the magnets. **M** is called the intensity of the magnetization, or the magnetic moment per unit volume. The specific magnetization, $\sigma$ is given by

$$\sigma = \frac{m}{w} = \frac{m}{v\rho} = \frac{\mathbf{M}}{\rho} \text{ emu/g}, \tag{1.2}$$

where $w$ is the mass and $\rho$ is the density of a material [1.6]. This specific magnetization is very likely to be utilized in biomedical application as well.

In atomic physics, there are two different sources of magnetic moments which are the orbital angular motion of the electron and the intrinsic spin angular motion of the electron. The spin of the electron is quantized in two possible orientations, 'spin-up' and 'spin-down'. This spin is a dominant source of the magnetic moment in an atomic scale and it is called the Bohr magneton ($\mu_B$ = $9.274\times10^{-24}$ $A\cdot m^2$ or $9.274\times10^{-21}$ erg/Oe). The specific properties of magnetic materials are determined individually by the magnetic moments of their atomic electrons. The total magnetic moment of an atom is a vector sum of the intrinsic moment of the electron and the orbital motion of the electron around the proton. The net moment of an atom is given by

$$\vec{m} = \frac{e}{2m_e c}\left(\vec{L} + 2\vec{s}\right) \tag{1.3}$$

where $e$ is the electron charge, $m_e$ is the electron mass, $c$ is the speed of light, $\vec{L}$ and $\vec{s}$ are the orbital angular momentum and the spin angular moment of electrons respectively.

### 1.1.3 Diamagnetism & Paramagnetism

If an external field is applied to each electron magnetic moments, mostly it will be aligned to the same direction of the magnetic field on average. However, atomic magnetic moments are not aligned in all magnetic materials. Commonly, electrons in an atom are arranged in pairs with equal number of north and south magnetic poles. Therefore, the magnetic moment from each electron is canceled out and this is owing to a result of the Pauli exclusion principle. Moreover, even when the electron configuration is unpaired or non-filled sub-shells, it often has zero net magnetic moment. According to the net magnetic moment of the electrons as well as the magnetic material's behavior on temperature, all substances can be classified into five categories: Diamagnetism, paramagnetism, ferromagnetism, ferrimagnetism and Anti-ferromagnetism. Diamagnetic and paramagnetic materials exhibit no magnetic interactions between atomic moments and are not ordered magnetically. Meanwhile, materials in the other three categories exhibit long-range magnetic order below their moments without critical temperature. Among them, ferromagnetic and ferrimagnetic materials have moments without applied field but the other three require a field, and are often called non-magnetic materials.

Diamagnetism is present in all materials and does not have an overall net moment. A diamagnet does not have orbital moment or unpaired spins. When a diamagnetic material is placed in a magnetic field, it tends to oppose an external magnetic field or turns out to be repelled by an applied magnetic field. This is represented by the susceptibility of each material. The susceptibility $\chi$, given in units of emu/(Oe·cm$^3$), is defined as the ratio of the magnetization to the applied field and it has negative value for a diamagnetic substance. This phenomenon describes the response of the core orbitals of all materials. However, the effect of

diamagnetism is overwhelmed by the much larger effects resulted from the unpaired electrons in paramagnetic and ferromagnetic substances.

In the case of paramagnetism, the atoms in the material normally have no net magnetic moment owing to the unpaired electrons. When a magnetic field is applied, the moments tend to align partially in the direction of the field. This magnetic property results in a net positive magnetization and also positive susceptibility even though the values are not large compared to ferromagnetic or ferrimagnetic materials. However, they return to a nonmagnetic configuration when the field is removed. In addition, many paramagnets are easily affected by temperature, this causes a temperature dependent susceptibility, well known as the Curie Law.

### 1.1.4 Ferromagnetism and Hysteresis loops

In 1906, Pierre Weiss proposed the first modern theory of ferromagnetism that there is a strong internal molecular field which is proportional to the magnetization of a ferromagnet below a certain temperature [1.7]. There are three transition metals that possess unpaired electron spins: iron (Fe), cobalt (Co), and nickel (Ni) and these transition metals are the main elements in the modern technology of magnetic applications. A strong exchange force occurs between the two atoms and causes unpaired spins. This is called quantum mechanical exchange forces which Heisenberg described by a special Hamiltonian [1.8]. The exchange forces result in a parallel alignment of neighboring spins and strong magnetization is formed inside a material. Ferromagnetic materials show two distinct characteristics. The first characteristic is spontaneous magnetization owing to the internal molecular field even in the absence of a field. The second characteristic is

temperature dependent magnetic ordering. Although the exchange forces of electrons are very strong, it is overwhelmed by thermal energy which randomizes the parallel alignment of spins. All ferromagnetic materials have their maximum temperature where they lose the ferromagnetic property as a result of thermal fluctuation. Eventually, the ferromagnet is disordered above the specific temperature and it is called the Curie temperature ($T_c$). Much research and experiments proved this type of behavior and characteristic of the ferromagnet [1.9], [1.10], [1.11].

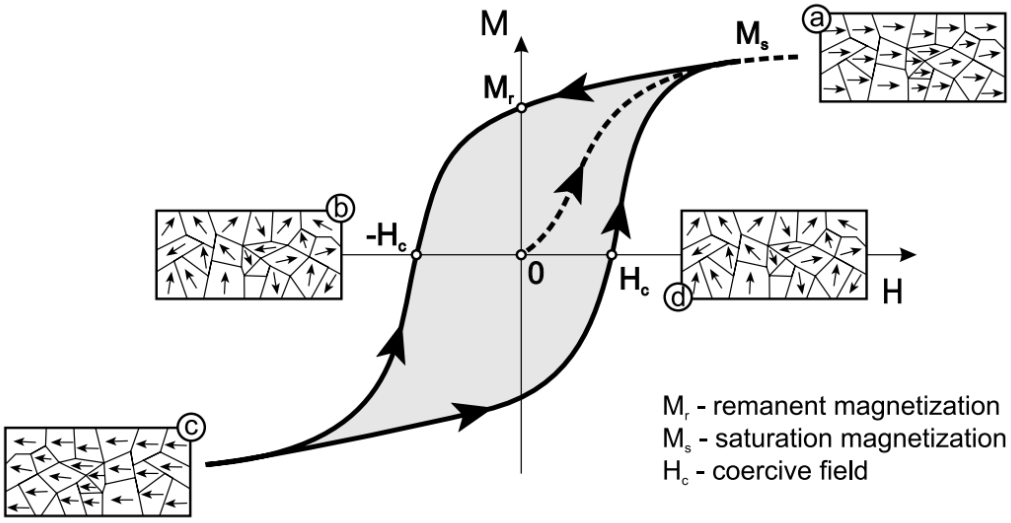


Figure 1.1: The magnetization '**M**' vs magnetic field strength '**H**' for a ferromagnetic material

(Source: http://www.fy.chalmers.se/edu/lab/labpm/em4_magnetic_hysteresis.pdf)

In addition to the saturation magnetization and the Curie temperature, an essential characteristic of the ferromagnetic material is the irreversible response of magnetization to an applied magnetic field. This lack of retrace-ability of

magnetization curve is called “hysteresis” and it is associated with the presence of magnetic domains in the material. Therefore, the unique property can preserve the magnetization status, i.e. a magnetic “memory” of the field, even after removing the applied field. This response is epitomized by the hysteresis loop and the variation of magnetization with the magnetic field is shown in figure 1.

The domain structures are depicted schematically on the hysteresis loop of Fig. 1.1 for the zero net magnetized state at the origin, the saturated state where $\mathbf{M} = \mathbf{M_s}$, the remanent state in zero applied field where $\mathbf{M} = \mathbf{M_r}$ and the state at $\mathbf{H} = \pm\mathbf{H_c}$, the coercive field at zero-crossing magnetization locations. Ferromagnetic materials have this very useful property that is used in magnetic storage devices such as a magnetic recording disk, recording tape, magnetic bar-codes, and so on.

### 1.1.5 Ferrimagnetism and Anti-ferromagnetism

Similar to the property of ferromagnetic materials, ferrimagnetic substances exhibit a substantial spontaneous magnetization below the Curie temperature, and become paramagnetic above this temperature. The magnetic structure consists of two magnetic sublattices which are often connected by oxygen. The most well-known ferrimagnetic material is ferrites. It was discovered by L. Néel who provided the critical theory to understand ferrimagnetism in 1948 [1.12]. At the same time, anti-ferromagnetic material was also classified by him. The electron spins in anti-ferromagnetic atoms are aligned in a regular pattern but pointing in opposite directions. Therefore, the anti-ferromagnetic substances have small positive susceptibility, however their susceptibilities vary with temperature. Antiferromagnets are paramagnetic above a certain critical temperature, called the Néel temperature, $T_N$. The common anti-ferromagnetic materials occur among

transition metal compounds such as hematite. It is often used with ferromagnets and this provides great advantages such as spin valve magnetic sensors, in magneto-resistive random access memory, as well as modern hard drive read heads.

### 1.1.6 Domain theory

The domain theory of ferromagnetism developed by Pierre Weiss argues that the large number of atomic moments is aligned parallel, but the direction of alignment varies from one domain to another. This phenomenon is commonly exhibited in ferromagnetic materials, even though they have their own crystalline anisotropy axes, called easy axes. The domain structure of ferromagnets is a result of minimizing the total free energy, in other words the domains have a tendency to form in the lowest energy state. Figure 1.2 graphically describes how domains are built in a large region of ferromagnetic material which is uniformly magnetized inside. At the beginning, the single domain element generates a large magnetic field spreading into the outer space. Therefore, the surface charges are stored on the both ends with positive and negative charges. This is called the magnetostatic energy and it can be defined as the volume integral of the field squared over all space. If the element is divided into two domains with the magnetization in opposite directions, the magnetostatic energy is reduced. Eventually, the lowest energy state can be reached which is the equilibrium domain configuration when it is cooled below the Curie temperature.

When a single domain transforms to a multidomain structure, the region between two adjacent domains having opposite magnetization directions is created, called a “domain wall”. This region between the domains is associated with the exchange interaction which strongly induces the parallel alignment of magnetic

dipoles in the same direction. Therefore the size of domain wall is proportional to the exchange energy however it is inversely proportional to the magnetocrystalline energy due to the demagnetizing field. Both exchange and magnetocrystalline energies exist along the length of the domain wall. In addition to the exchange interaction energy responsible for the parallel alignment of adjacent atomic moments, many components such as magnetostatic energy, anisotropic energy, and magnetoelastic energy contribute to the domain formation as well. More detailed explanations about the critical energy components will be given in the subsequent sections.

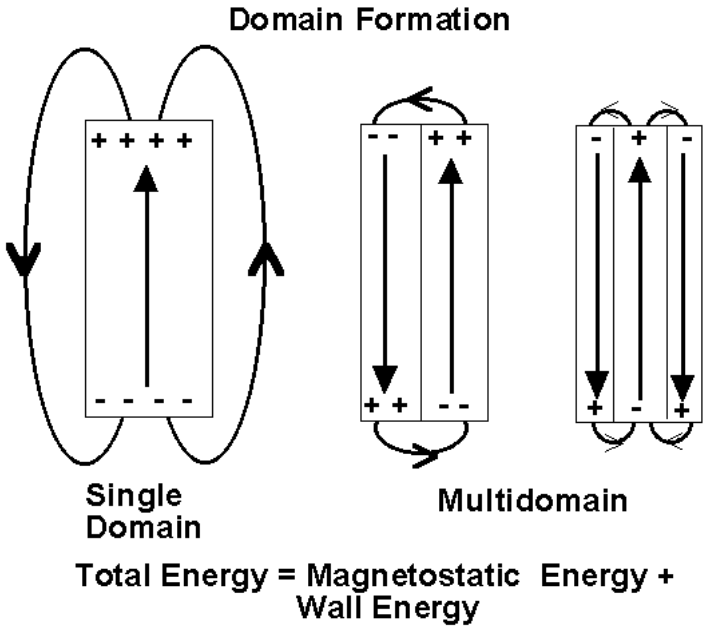


Figure 1.2: Formation of single magnetic domain and multi-domain

(Source: http://www.splung.com/content/sid/3/page/magnetism)

As the size of a ferromagnetic particle decreases sufficiently, the particle could only hold one domain which has the lowest energy of all possible states.

There is a size range for a single domain particle which is approximately less than 100 nm. Within this size range, the total volume of the particle is so small that it is subject to thermal agitations. Therefore below the certain diameter, "d" of a particle (d < 100 nm), thermal agitations can cause the random magnetization directions of a single domain particle which is called "superparamagnetism" and above a certain size (d > 100 nm), a single domain particle will begin to build a multi-domain structure.

## 1.2 Magnetic recording

### 1.2.1 Overview

Magnetic recording has been with us for over a century. In 1888 Oberlin Smith implied the possibility of magnetic recording using cotton threads in which steel dust would be suspended. Ten years later, the 'telegraphones' was the first magnetic recorder invented by the Danish engineer, Valdemar Poulsen in 1898. Afterwards, a few technologies of magnetic analog recording such as analog audio tape recording (by AEG and BASF in 1930) and video recording (by AMPEX in 1956) were developed. Often through the successive development of analog recording technologies, digital recording world began to grow as the next generation in magnetic recording industry. IBM was proud to be in the vanguard of decisive innovation among magnetic storage industries. They introduced the original RAMAC (random access method of accounting and control) based on a pile of 50 two-sided 24 inch disks. It was the first commercial hard disk drive having a random access feature by using a moving head over the disk surface. It

had an areal density of 2 kbit/in$^2$, a data rate of 70 kbit/s, and a storage capacity of 5 Mbytes [**1.13**]. Compared to RAMAC, a modern 3.5 inch hard disk drive is the direct descendent and provides 1 Tbyte of storage which is a significant improvement in areal density and cost per byte of approximately eight orders of magnitude.

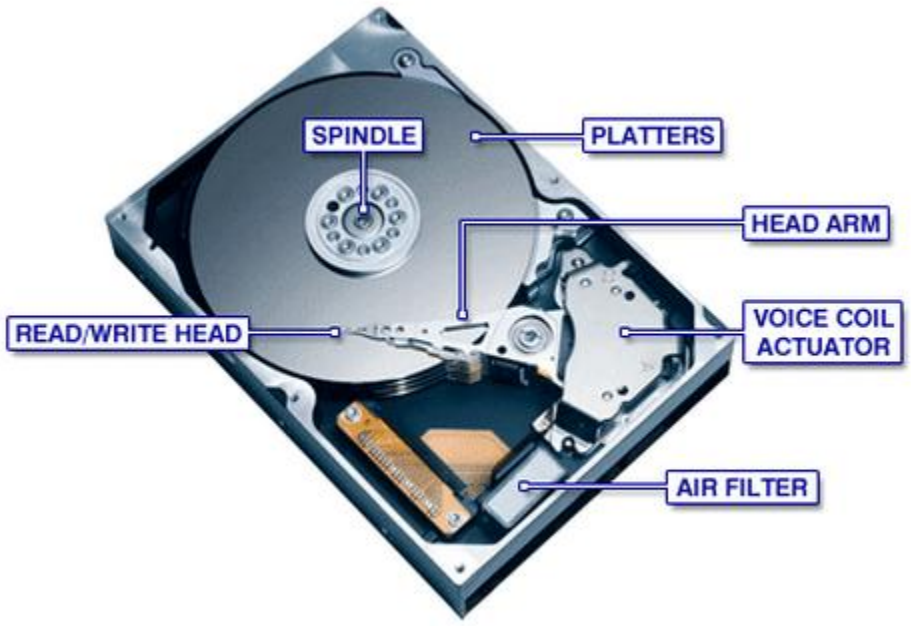


Figure 1.3: A typical hard disk drive (HDD) inside image with labeling main components (Source: http://news.bbc.co.uk/2/hi/technology/6677545.stm)

Fig. 1.3 shows the overall structure internal of a hard disk drive with the labels of main components. A typical hard disk drive is composed of platters, a motor, a spindle, read/write heads, an actuator and electronics. A hard disk drive has at least one or more platters (or disks) to store data and each platter has a head on both top and bottom sides. The platters are made from non-magnetic materials,

such as glass or ceramic, but have magnetic thin film coating layers on both sides for the purpose of magnetic recording. All the platters are mounted on the spindle which is rotated by a spindle motor. The rotation speed of a motor for current commercial products varies from 4,200 RPM in portable devices to 15,000 RPM for high performance servers. The read/write heads mounted on a slider fly only a few nanometers above the surface of the platters. When the read/write heads fly on the spinning platters, they record magnetization patterns, called bits, or read back from the previously recorded magnetization patterns on the media. The sliders having read/write heads are connected to the triangular-shaped head arm. The head arm enables the sliders to move from the hub to the edge of the drive. Each slider is controlled by a separate head arm and all of them are lined up and mounted to the actuator axis as a single unit. The head arm is controlled by a voice coil actuator which has very accurate track seeking ability. In addition, the air filter removes any leftover contaminants from the manufacturing process and any particles or chemicals that may have entered inside the hard drive enclosure.

One of the competing data storage devices is a solid-state drive (SSD) that uses integrated circuit assemblies as memory to store information. Most current SSDs are based on NAND Flash memory which is non-volatile. Compared to hard disk drives, the advantages of SSDs are fast access, resistance to impact and vibration, low power consumption, high reliability, and low noise during operation. Back in 1965, Gordon E. Moore described a rule of thumb in the history of computing hardware: the number of transistors on an integrated circuit doubles every two years at a minimum cost per transistor [1.14]. This is called Moore’s law and his prediction has proved to be keenly accurate for research and development in the semiconductor industry. Recently, IM Flash Technologies (IMFT), a joint

venture of Intel and Micron for process development, announced the development and manufacture of high density multi-level NAND Flash memories with a 20 nm process technology for the first time. The areal density growth rates of the NAND Flash memory were in the 40 % to 100 % range up to the present time. However, the semiconductor industry is confronting a challenge to follow Moore's law because extreme ultraviolet lithography will require the new ecosystem for photoresists, mask tooling, defect detection and so on. Therefore, the technology roadmap shown in Fig. 1.4 is going into a highly unclear stage, even though flash storage market industry may increase rapidly in the next decade [1.15].

Compared to the NAND Flash areal density history, the HDD areal density growth rates have shown a similar tendency ranged from the 40 % to the 100 % over the last two decades. Many innovative technologies have been introduced in every change of the growth rate improvement. One of the important advancements has been the magneto-resistive (MR) head. The 1$^{st}$ anisotropic magneto-resistive (AMR) head was introduced in 1990 and a following technology was giant magneto-resistive (GMR) head in 1997. Originally, GMR effect was discovered in 1988 by Fert and Grünberg who received the Nobel Prize in 2007. Also a new type of magnetic recording media such as the anti-ferromagnetically coupled (AFC) media was developed in 2001. After that, the second generation recording technology, called perpendicular magnetic recording (PMR) was introduced in 2004, even though the fundamental concept of PMR was proposed in the late 1970s to overcome potential problems with longitudinal recording [1.16, 1.17]. Fig. 1.4 shows the areal density growth rate and perspective of the hard disk drive compared to that of Flash memory. Similar to the growth rate of the Flash products,

the annual growth rate of the hard disk drive products shows relatively slow increase from 2000.

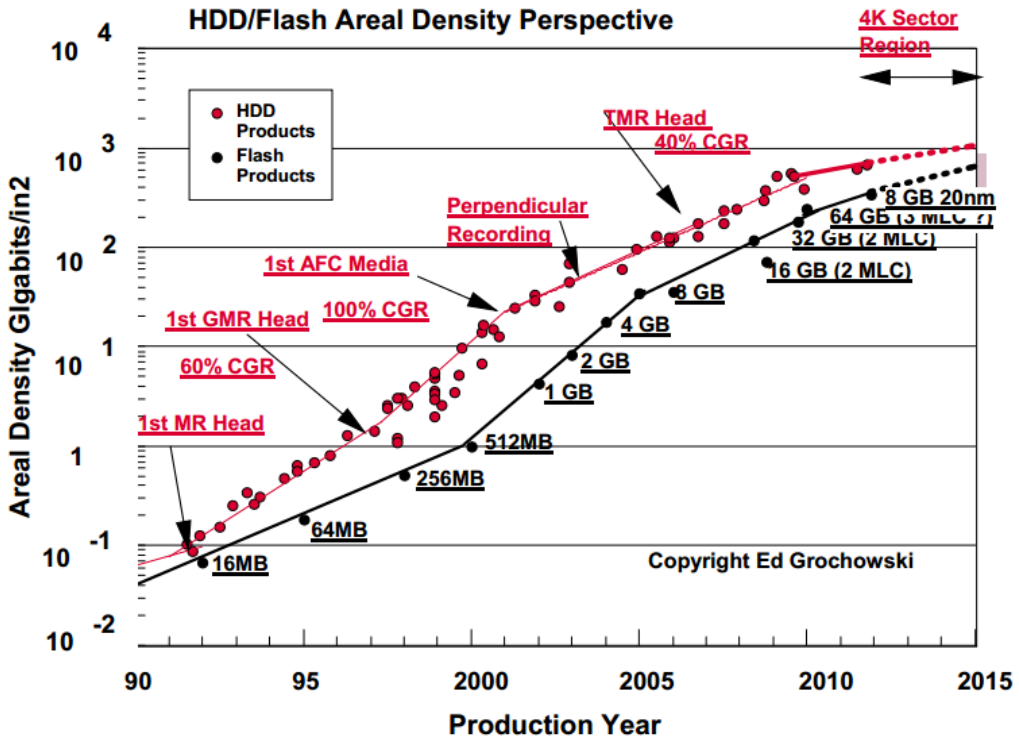


Figure 1.4: Areal Density History for Roadmap of HDD and NAND Flash (Source:http://www.flashmemorysummit.com/English/Collaterals/Proceedings/2011/20110809_F2C_GrochowskiFontana.pdf)

Until hard disk drives using perpendicular magnetic recording (PMR) were commercially available, longitudinal magnetic recording (LMR) was the standard recording methodology of hard disk drives for over 50 years. As the name of LMR describes, the magnetizations of data bits prefers to be aligned horizontally in the spinning direction of the recording media. The magnetizations were written by the longitudinal stray fields generated from the “Ring” inductive writing head shown in

Fig. 1.5(top). The stray field leaking out of the head is not very strong. Meanwhile, the fields between two adjacent bits with opposing magnetizations are separated by a relatively large transition region due to the energetically unstable state. Despite the fundamental disadvantages described previously, over the years many technological developments to LMR were achieved. As a result, the areal density of LMR increased rapidly. However, at the end of the 1990s, the steady recording areal density improvement of LMR was prevented by fundamental limitations such as superparamagnetism, and insufficient head field from ring-shape write heads [1.18]. Therefore, the traditional growth rate of LMR areal density was not able to maintain and eventually slowed down beginning in 2002. The highest areal density for LMR was about 130 $Gb/in^2$ in early 2000s [1.19].

Even though many efforts were made to realize PMR technology, the magnetic recording industry was not successful until the early 2004. Unlike LMR, the preferred axis of the magnetization for PMR is normal to the surface of recording media. There are many advantages of the perpendicular recording system over the longitudinal recording. The $1^{st}$ benefit is higher thermal stability that can be achieved by small grain diameter with larger grain thickness than grain diameter. The $2^{nd}$ advantage results from a perpendicular single pole head with a soft underlayer which enables to generate almost double the field of longitudinal recording head. In addition, the soft underlayer gives a guide for the head flux to go back into the return pole. This allows increasing the coercivity of the medium having smaller grain size. The $3^{rd}$ advantage is the smaller demagnetization field at the transition region. Thus, narrower magnetic transition helps to increase recording areal density. The other benefit is less noise at the track edges in the media due to the vertical pole head configuration. It also allows higher track

density and a smaller bit aspect ratio. Therefore, PMR has begun replacing LMR from 2004 and delayed the superparamagnetic effect: however, superparamagnetism was not resolved completely.

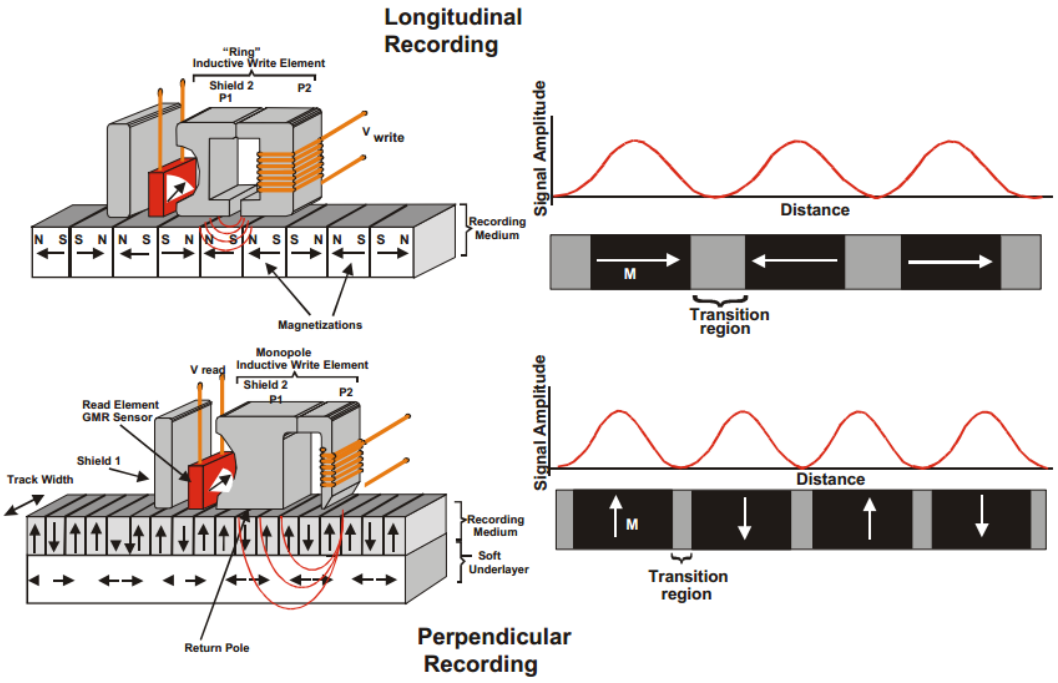


Figure 1.5: Schematic view of the recording head and media structure and signal amplitude from magnetic transitions for longitudinal magnetic recording (top) and perpendicular magnetic recording (bottom).

(Courtesy of Hitachi Global Storage Technologies)

## 1.2.2 Technical challenges for higher density recording

The structures of a hard disk drive (HDD) head (write & read) and recording media are designed and fabricated by sequentially depositing various kinds of films to achieve high areal density. In the recording layers' point of view, increasing areal density means that the performance of the recording layers should

be improved. In other words, the size of the single-domain particles in the medium should be reduced and more uniform, while maintaining the signal to noise ratio (SNR). In addition, the crystalline anisotropy directions of the grains should be improved to decrease noise. The smallest magnetic units are the grains and the stored energy in one grain can be described by $\boldsymbol{K_u V}$, where $\boldsymbol{K_u}$ is the magnetic anisotropy energy density considering both crystalline and shape anisotropies and $\boldsymbol{V}$ is the volume of a grain. The anisotropy energy of a grain must be larger than the thermal energy $k_{\mathbf{B}}\boldsymbol{T}$ ($k_{\mathbf{B}}$: Boltzmann's constant = $1.38\times10^{-16}$ erg/K) in order to avoid spontaneous magnetization reversals between two local minimum energy states. Over fifty years ago, Nobel prize winner Louis Néel established the theoretical basis for the possibility of magnetization reversal which relates reversal rate $\boldsymbol{r}$ to volume $\boldsymbol{V}$, the anisotropy constant $\boldsymbol{K_u}$, and the absolute temperature $\boldsymbol{T}$ [1.20]. The theory is expressed as

$$r = f_0 e^{-\frac{\Delta E}{k_B T}} \tag{1.4}$$

where $f_0$ is the attempt frequency and $\Delta\boldsymbol{E} = \boldsymbol{K_u V}$ is the magnetic energy barrier. Based on this equation, the possibility of magnetization reversal of a particle is given by the ratio of magnetic energy barrier to the thermal energy. When a particle having an initial magnetization is placed at an environment without ambient magnetic field, the anisotropy energy maintains the magnetic moment in its original direction and the magnetization will not change over time. However, at some temperature, the magnetization orientation of the particle may change over time as a result from receiving thermal energy. Therefore, the magnetization as a function of time will decay and eventually will be reversed. The governing equation for the decay is defined as

$$M(t) = M_i e^{-rt} \tag{1.5}$$

where $t$ is time and $M_i$ is the initial magnetization of the particle. The inverse of the reversal rate $1/r$ is called the relaxation time $\tau$. In a magnetic recording system, if we want to keep the stored magnetic information for a long time, the relaxation time should be as long as possible. For instance, the attempt frequency of current recording media is equal to $10^{11}$ Hz and if we want to keep the data at least over 10 years, then the ratio of the energy barrier to thermal energy $\boldsymbol{K_u V}/k_B \boldsymbol{T}$ should be larger than 45 at room temperature. Therefore, the anisotropy energy of each magnetic particle must be large enough to avoid spontaneous reversals of magnetization which lead to thermal decay and superparamagnetism.

Based on the description of the stored energy in the previous paragraphs, the magnetic energy of a grain can be maintained even at smaller grain size if the anisotropy energy density is increased accordingly. As the anisotropy energy increases, higher write head field is required in order to flip the magnetization. However, the field generated by a write head is limited by the magnetic moment of the head material as well as the head design structure. The current dominant magnetic material of a write head is "FeCo" alloy having the maximum saturation moment $B_s$ ($=4\pi M_s$) of 2.4 Tesla. Therefore, the design of higher areal density recording media is prevented either from the thermal instability of small grain size, the necessity of high write field due to the high anisotropy field or by insufficient SNR due to the large grain size. In magnetic recording industry, this is called the "Trilemma" of magnetic recording in order to indicate that there are three undesirable main issues [1.21]. Fig. 1.6 shows a diagram of recording media trilemma and the three corners of the triangle diagram are incongruous states.

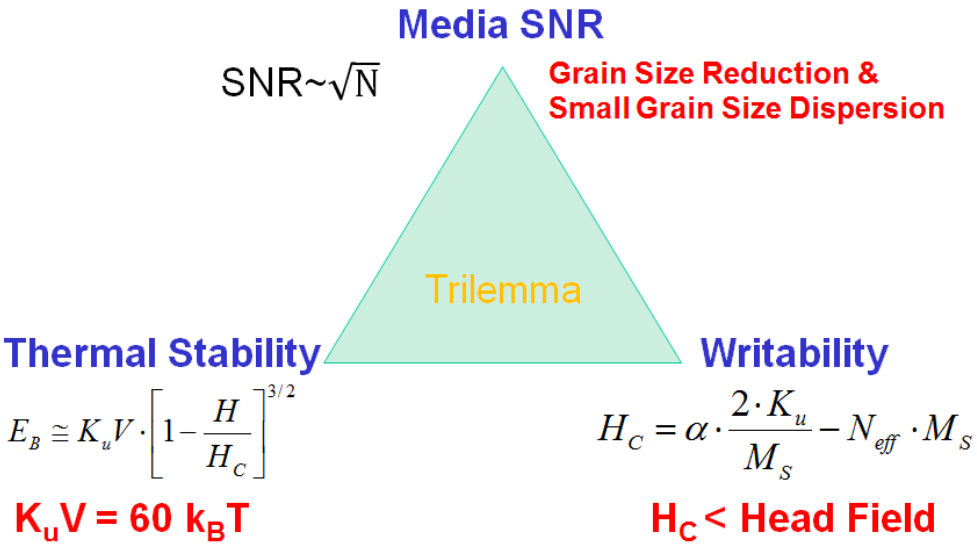


Figure 1.6: Diagram of the recording media trilemma in magnetic recording industry

### 1.2.3 Write head

The writer of the traditional magnetic recording is a ring type head creating the longitudinal transitions by the down-track components of the stray field from the write gap. Therefore, the saturation magnetization of the head and the fraction of the field delivered to the recording layer limit the coercivity that can be used in the media. In perpendicular magnetic recording, a single pole head combined with a highly permeable soft underlayer (SUL) requires a return pole or a trailing shield, as in Fig. 1.7. The SUL is physically part of the recording medium, but magnetically belongs to the write head. The recording layer is deposited on top of a SUL that draws sharply the flux from the single pole head and guides it to the return pole. Therefore, a SUL becomes a part of the head structure and the behavior of the SUL is well understood from the principle of image charges which makes the head field double ideally. The magnetic field is generated by the surface of the

main pole tip and delivered to the medium. The produced flux, which circulates along the magnetic circuit including the main pole, the SUL and the return pole, is conserved:

$$\Phi = A_{\mathrm{mp}} B_{\mathrm{mp}} = A_{\mathrm{rp}} B_{\mathrm{rp}} = A_{\mathrm{SUL}} B_{\mathrm{SUL}}\,, \tag{1.6}$$

where $A_{\mathrm{mp}}$ is the bottom surface of the main pole, $B_{\mathrm{mp}}$ the flux density at the main pole, $A_{\mathrm{rp}}$ the bottom surface of the return pole, $B_{\mathrm{rp}}$ the flux density at the return pole, $A_{\mathrm{SUL}}$ the relevant area of the SUL [1.21]. The relationship implies that the bottom surface of the trailing shield should be much larger than that of the main pole in order to avoid overwriting other bits.

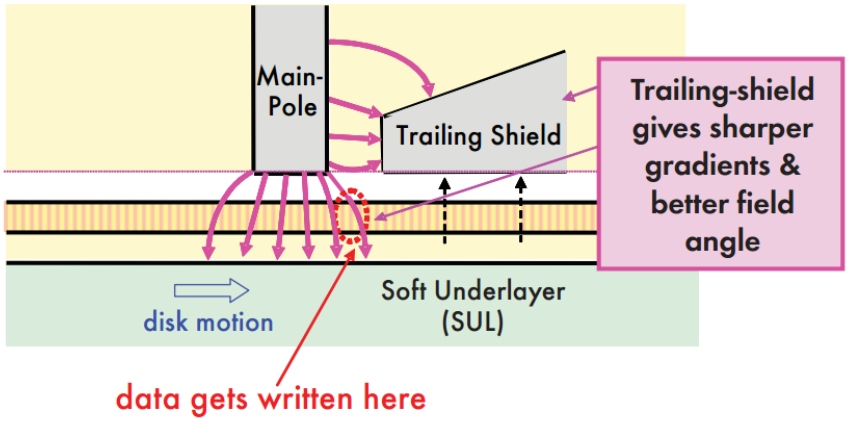


Figure 1.7: Cross-sectional schematic of a perpendicular single pole head with a "trailing shield" placed in the proximity of trailing edge of the writing pole (Source:http://www.hgst.com/tech/techlib.nsf/techdocs/F47BF010A4D29DFD8625716C005B7F34/$file/PMR_white_paper_final.pdf)

In addition to the major role of flux guidance, the trailing shield is used to increase the head field gradient in the down track direction. This higher field gradient assists to decrease bit length thus it gives higher signal to noise ratio as

well as a higher linear density [1.22]. The position of data which will be written between a main pole and a trailing shield is shown in fig. 1.7. One possible disadvantage for a trailing shield might be the leakage flux directly transferring from the side of a main pole to the trailing shield as a short-cut. If the gap between the main pole and the trailing shield is too small, then this will cause serious reduction of the head field strength right under the main pole. Therefore, when a write head with a trailing shield is designed, head field strength and field gradient must compromise with each other. As a rule of thumb, the gap between them is supposed to be similar to the space between the air bearing surface and SUL. Theoretical aspects and experimental implementations of a head having a trailing shield have been investigated in [1.23], [1.24].

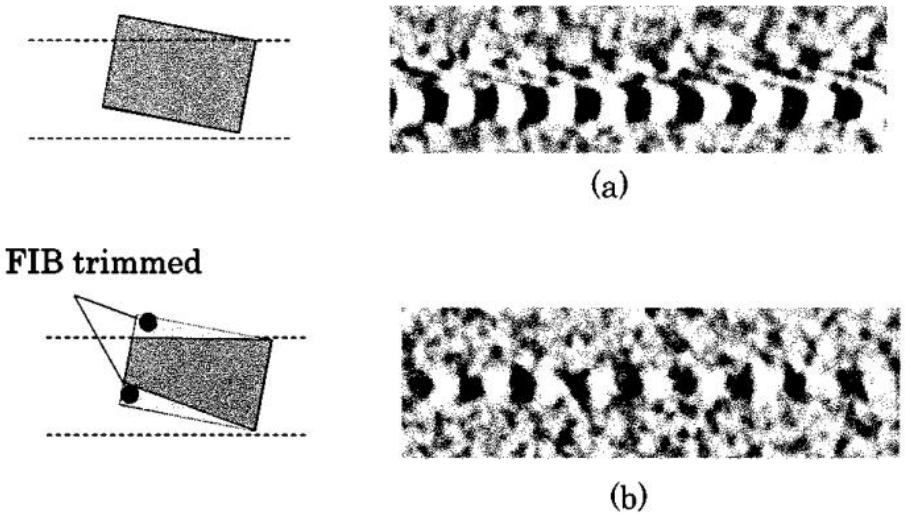


Figure 1.8: MFM images of recorded bits (a) Recorded with conventional SPT writer. (b) Recorded with a focus-ion-beam (FIB) trimmed SPT writer with trapezoidal shape main pole [1.25].

Similar to a trailing shield, side shields should be considered for preventing adjacent track erasure (ATE). Even though the leakage flux in the cross track direction from the narrow writer is much weaker than the nucleation field of the medium, the adjacent track is possible to be erased after encountering many passes combined with thermal fluctuation field. A typical write head pole has a rectangular shape with the pole length at least 2 times larger than the cross track dimension for providing sufficient write fields. Generally, the corner of the writer produces strong stray field and the skew angle between the axis of the recording head and the circumference of the track is designed to be in the range of +10 to +15 degrees at the inner disc diameter and -10 to -15 degrees at the outer diameter. When the writer is used at skew, the corner of a rectangular shape pole tip will be off-track and protrude to the adjacent tracks. This problem will cause ATE or the written transition widths will be too wide. Therefore, the head of a narrow trapezoidal shape with well controlled angle has been developed and reduces the skew asymmetry as well as ATE [1.25], [1.26]. Fig. 1.8 shows the MFM images of recorded bits with a rectangular shape single pole tip (SPT) writer and a trapezoidal shape SPT writer. The other issue related with writer is on-track erasure owing to the remanence of a write head. Those issues should be considered with the design of a single pole head with SUL for high density recording [1.27].

### 1.2.4 Read head

Magnetic recording readers are based on the principle of magnetoresistance. When a magnetic field is applied to a material, the value of its electrical resistance is changed. The ordinary magnetoresistance was discovered by William Thomson in 1856 however, the electrical resistance of a material was not changed much at

the beginning. Anisotropic magnetoresistance (AMR) was the first commercialized property of a material. In AMR, electrical resistance depends on the angle between the external magnetic field and the electric current direction. The maximum electrical resistance is observed when the direction of the magnetic field is parallel to the direction of current. AMR has been obtained up to 50 % for some ferromagnetic uranium compounds [1.28].

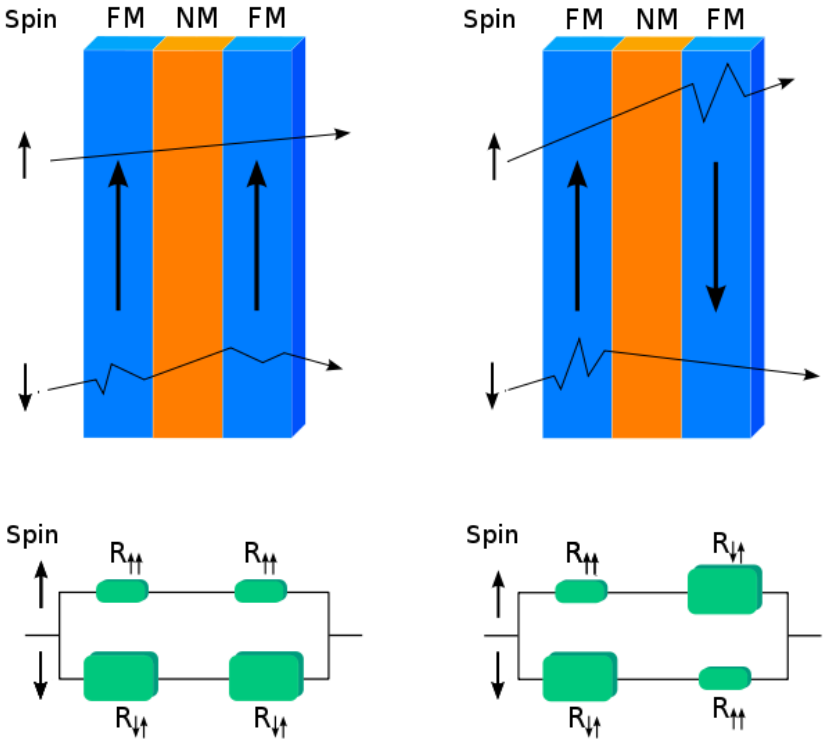


Figure 1.9: Illustration of CPP GMR structure: the parallel configuration on the left and the anti-parallel configuration on the right with equivalent electric circuit representations, respectively

(Source:http://en.wikipedia.org/wiki/Giant_magnetoresistance)

Continuously, the MR technology has been improved and extended to the giant magnetoresistance (GMR) and the tunneling magnetoresistance (TMR). GMR is observed in the structures of magnetic metal layers separated by a nonmagnetic metal layer. It is possible to reorient the magnetic moments of the ferromagnetic layers relative to one another. These structures include magnetic multilayers, spin valves, and granular solids. An early example of the GMR effect anti-ferromagnetically coupled ultra-thin Fe/Cr multilayers separated by a non-magnetic metal layer [1.29]. The interlayer exchange coupling is caused by electrons near the Fermi level: It oscillates with separation distance. According to the thickness of the nonmagnetic spacer, it is possible to generate an anti-parallel configuration of the ferromagnetic layers and then align the magnetic moments by an external field. In a spin valve, the magnetization of one ferromagnetic layer is pinned by the exchange coupling with a neighboring anti-ferromagnetic layer, while the magnetization of the other ferromagnetic layer is free to rotate with the applied field [1.30]. For the magnetic recording read head, the free layer of magnetization is rotated by the external field from the media transitions. The spin valve GMR has two types of structures, current in plane (CIP) and current perpendicular to the plane (CPP), depending on the direction of current flow. CPP GMR configurations are illustrated in fig. 1.9. A parallel configuration is shown on the left and an anti-parallel configuration is shown on the right with equivalent electric circuit representation, respectively. The different magnetization alignments of the GMR structure provide different resistances due to the various scattering rates of spin up or spin down electrons. Each configuration describes two spin states (spin up and spin down) passing through the structure with different scattering rates. For example, if the spin of the electron is opposite to the direction of the magnetization in the

ferromagnetic (FM) layer, the scattering effect is larger than the parallel direction of the magnetization. This effect is known as the two channel current model [1.31]. Therefore, an equivalent electric circuit can be induced from this principle of electron scattering mechanism. The size of resistor illustrates the amount of resistance and the equivalent resistance for each configuration can be obtained.

Tunneling magnetoresistance (TMR) is selected to spin valve GMR. The spin up or spin down electrons pass through an insulating barrier (MgO) instead of the nonmagnetic spacer. Typically TMR has a larger MR value since it allows only majority electrons to pass the insulating barrier, called a "spin polarized effect". The effect of TMR was originally discovered in 1975 by M. Julliére however the resistance change was around 14 %. Recently, the effect of TMR has been increased up to 600 % at room temperature and over 1100 % at 4.2 K for junctions of CoFeB/MgO/CoFeB [1.32], [1.33]. This large advantage attracts more applications such as high performance and nonvolatile solid-state magnetic random access memories (MRAM), and TMR based read head for high density recording.

### 1.2.5 Recording media

Along with the technical development and analyses of magnetic write and read heads, a magnetic recording layer is critical component and has been progressed continuously. In similar to the final goal of the technical improvement of magnetic write and read heads, the primary goal of magnetic recording media is to raise the areal recording density. Therefore, the major categories for a good recording medium have to be an agreement among three parameters which are high recording density, high signal to noise ratio, and sufficiently high thermal stability. In order to satisfy the agreement of the above categories, a number of magnetic

parameters should be improved. For example, the transition parameter α should be reduced to increase a recording density. It is mainly proportional to the remanence-thickness product $M_r\delta$ of the medium and inversely proportional to the coercivity of the medium. These magnetic and structural parameters are dependent on one another.

As a result of the rapid growth rate of recording density (60 to 100 % annually) for the past decade [1.34], the longitudinal magnetic recording media eventually confronted the superparamagnetic limit. Hence, the longitudinal recording method was changed to the perpendicular magnetic recording method due to the tradeoff between high signal to noise ratio and thermal stability in the early 2000s. Historically, the first generation of a magnetic recording layer was composed of closely packed magnetic particles, called as a particulate medium. The representative magnetic particles are iron oxide alloys having a low saturation magnetization and low coercivity. For high density recording, there are a couple of fundamental requirements: high remanent magnetization with small media thickness, high coercivity, squared hysteresis loop, smooth surface and reliable mechanical stability and small as well as uniform grains. First of all, high remanent magnetization provides large enough readback signals and small media thickness minimizes the thickness spacing loss. High coercivity and squared hysteresis loop are very important to achieve the sharp transitions and the satisfactory overwrite ratio. The smooth surface and reliable mechanical stability provide to attain small magnetic spacing with acceptable tribological performance. Small and uniform grains mainly result in low transitional noise therefore, signal to noise ratio can be maintained while increasing recording areal density.

The second generation of magnetic recording media was thin film disks introduced in the late 1980s. In the early stage, the magnetic thin film disks are complex multilayer structures comprising of typically glass or aluminum substrate, amorphous NiP undercoat, chromium or Ni-based alloy underlayer, Co-based alloy magnetic film, carbon overcoat, and lubricant. The most critical component of a thin film disk is the magnetic recording layer. The current method of perpendicular magnetic recording has been used for commercial products since the mid-2000s. Ideally, the magnetic recording layer requires high coercivity and high magneto-crystalline anisotropy grains which are very uniform in size, much smaller than recording bit cells and magnetically isolated with nonmagnetic grain boundary. The material of primary magnetic recording layer is based on cobalt alloys. The initial Co-based alloys with a hexagonal close packed (hcp) for recording media include CoCrTa, CoCrPt, CoCrPtTa, CoNiCrPt, etc. [1.35], [1.36], [1.37]. The added elements assist to increase coercivity, to reduce the intergranular exchange coupling energy, and to enhance corrosion resistance.

The structure of perpendicular magnetic recording (PMR) media consists of a soft underlayer (SUL), seed layer, magnetic recording layer, and carbon overcoat layer. The greatest advantage of the PMR can be obtained from a SUL. The SUL doubles the write field strength as well as the head field gradient however it also generates the spike noise as well. Therefore, a single pole head combined with a SUL allows magnetic recording media to use high anisotropy recording materials for high coercivity and thermal stability. The spike noise can be detected by the read head and it comes from the magnetic multi-domain structure of a SUL. In order to minimize the noise, there are two useful structures: the anti-parallel structure SUL (APS SUL), the anti-ferromagnetism SUL (AFM SUL) [1.38]. The

APS SUL is composed of multiple soft magnetic layers with very thin nonmagnetic spaces between them. Thus, magnetic flux from the domain wall would not come out but circulate into the anti-parallel coupled neighboring soft magnetic layer. The AFM SUL is composed of a soft magnetic layer adjacent to an anti-ferromagnetic material layer therefore the magnetization of the SUL is headed to one direction by a bias magnetic field in the anti-ferromagnetic region. This structure controls the spike noise due to not having magnetic domain wall.

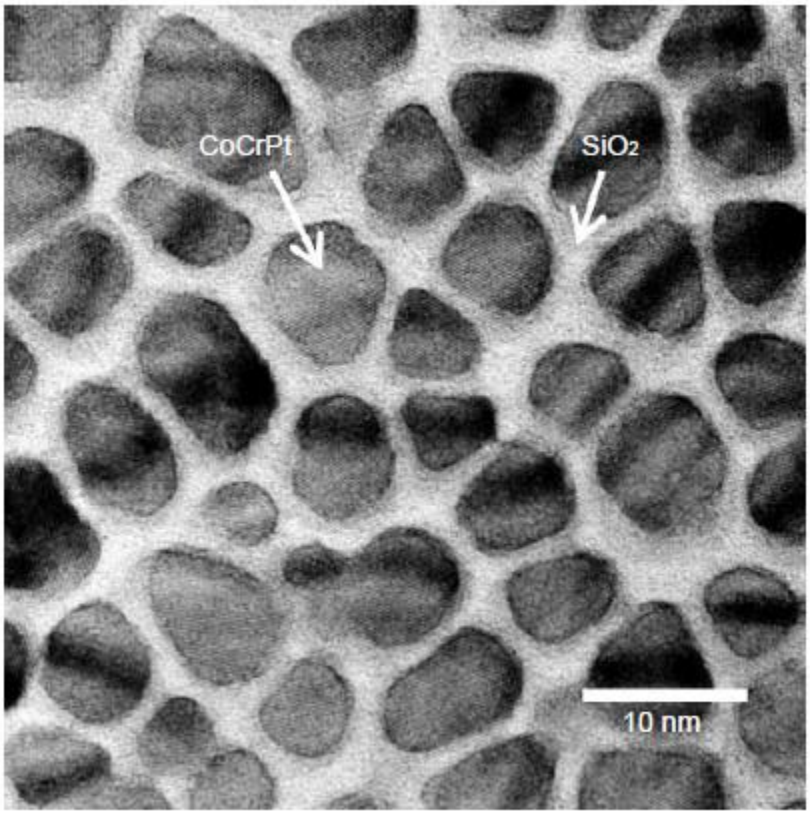


Fig. 1.10 In-plane TEM image of CoCrPt-$SiO_2$ layer [1.42]

Another method to reduce magnetic recording media noise is the separation between neighboring grains. For instance, CoCrPt-O and CoCrPt-$SiO_2$ granular material systems diminished the recording media noise owing to the reduction of

magnetic interaction between magnetic grains with O or $SiO_2$ [1.39], [1.40], [1.41]. An in-plane transmission electron microscopy (TEM) image of a CoCrPt-SiO2 granular recording layer is shown in fig. 1.10 and this separation between grains was achieved at room temperature. The other important issue is the easy axis distribution of the Co-based alloy grains. It was very difficult to control the epitaxial growth of the granular material before Ru is used as the interlayer of the perpendicular recording media. The distribution of the easy axis in normal direction in the CoCrPt-$SiO_2$ medium was 4 degrees or less and further it has been improved by using high gas pressure deposition of a Ru interlayer.

# Chapter 2 Micromagnetics

In this chapter, we discuss the micromagnetic model which has been used for the simulations through the whole of the dissertation. Landau and Lifshitz first proposed a micromagnetic theory in a paper in 1935 [2.1] and William Fuller Brown contributed largely to the theory called "Micromagnetics" in 1963 [2.2]. Micromagnetics is capable of providing the fundamental understanding of magnetization reversal processes on the sub-micrometer length scale since it deals with the interactions between magnetic moments and predicts the behavior of magnetic material taking into account its structure and intrinsic properties. Thus, micromagnetics is very useful to investigate the characteristics of biomagnetic nanoparticles, magnetic recording performance, and optimal design of a magnetic recording system. In order to build a model with statistical accuracy for those micromagnetic applications, the correlations among a few major governing energy terms of a magnetic moment should be clearly understood and analyzed. Based on purely classical and quantum mechanical theories, the governing energies consist of magnetostatic energy, magnetocrystalline anisotropy energy, exchange energy, Zeeman energy, and thermal energy. The generation of realistic grains and the modeling method will be introduced and each energy term will be presented.

## 2.1 The Landau-Lifshitz-Gilbert Equation

In magnetic material, the direction of magnetization can be varied dynamically by means of the effective field $\mathbf{H}_{eff}$. From quantum mechanics, it is

known as the dynamic precession of the spin magnetic moment around the field. Therefore, by combining the elementary volume and magnetization vector field **M**, the first dynamical model for the precessional motion of the magnetization was:

$$\frac{d\mathbf{M}}{dt} = -\gamma \mathbf{M} \times \mathbf{H}_{eff} \tag{2.1}$$

where $\gamma = 1.76 \times 10^7$ [$Oe^{-1} \cdot s^{-1}$] is the gyromagnetic ratio of the free electron spin. This is the Landau-Lifshitz equation that is a conservative Hamiltonian equation. However, the magnetization of real magnetic materials will be converged eventually in the effective field direction. Thomas Gilbert introduced phenomenological dissipation that depends on a damping constant α. This occurs by a kind of viscous force and the Gilbert damping constant is ranged from 0.001 to 1.0 depending on the material. Therefore, the dynamic motion of the magnetization is generally described by the Landau-Lifshitz-Gilbert (LLG) equation:

$$\frac{d\mathbf{M}}{dt} = \frac{\gamma}{1+\alpha^2}\mathbf{M} \times \mathbf{H}_{eff} - \frac{\alpha\gamma}{(1+\alpha^2)M_s}\mathbf{M} \times \left(\mathbf{M} \times \mathbf{H}_{eff}\right) \tag{2.2}$$

where $M_s$ is the saturation magnetization. The first term on the right hand side represents the gyromagnetic precession of the magnetization, also called "Lamor precession", with an angular frequency of $\omega=\gamma H$ when the damping constant is zero. The second term is a damping term which makes the magnetization of material eventually converge to the same direction of the effective field. Figure 2.1 illustrates the dynamic relations between the precessional motion and energy dissipation.

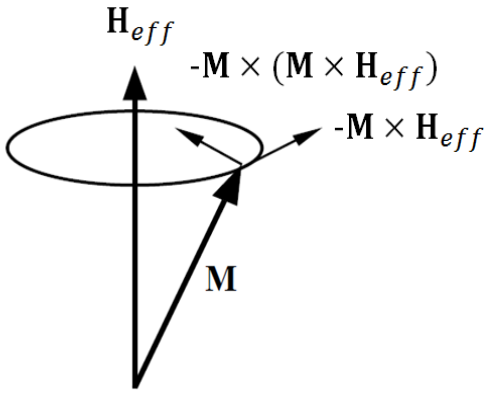


Figure 2.1: Magnetization dynamics having damped gyromagnetic precession.

Both terms are orthogonal to the magnetization direction due to the cross product $\mathbf{M} \times \mathbf{H}_{eff}$ and thus, the amplitude of the magnetization is preserved. With the LLG formula (2.2), the dynamic behavior of the magnetization is able to be numerically computed by a differential equation with an appropriate time step. In application to bio-magnetic nanoparticles or typical magnetic recording systems, the saturation magnetization and the damping constant are considered time invariant throughout the computation.

## 2.2 Grain Geometric Configuration

As the TEM image of recording layer shows in figure 1.10, the perpendicular magnetic recording (PMR) layer has a complicated morphology. Therefore, it is difficult to reproduce and analyze accurately real grains by using a micromagnetic model. For instance, the assumption of regular grains such as spherical or hexagonal grains may be helpful to describe the real grain system

however they are still insufficient to describe in detail the interactions between adjacent grains. The real grains of a PMR layer have irregular shapes and non-uniform size distribution. In addition, recording media is often governed by non-uniformity of magnetic moment or magnetic cluster owing to the inter-granular exchange interaction.

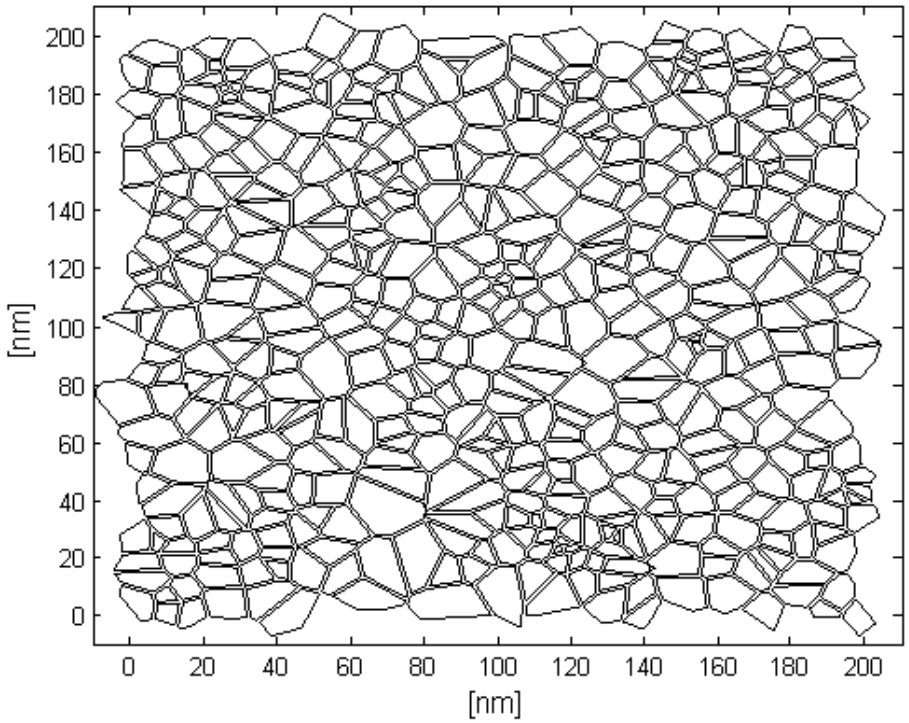


Figure 2.2: A schematic diagram of an array of 500 grains generated by planar Voronoi cells.

In order to represent the complicated grain morphology, we used non-uniform Voronoi unit cells which consist of randomly distributed polygons in two-dimensional space [2.3]. One of the advantages of this scheme is able to simulate the exchange interaction between adjacent grains and also make it possible to

consider the non-uniform grain size distribution on recording layer characteristics. Another benefit is that we can easily control the average grain size and the grain size distribution. The Voronoi unit cells follow a log-normal distribution which is very similar to the real grain size distribution.

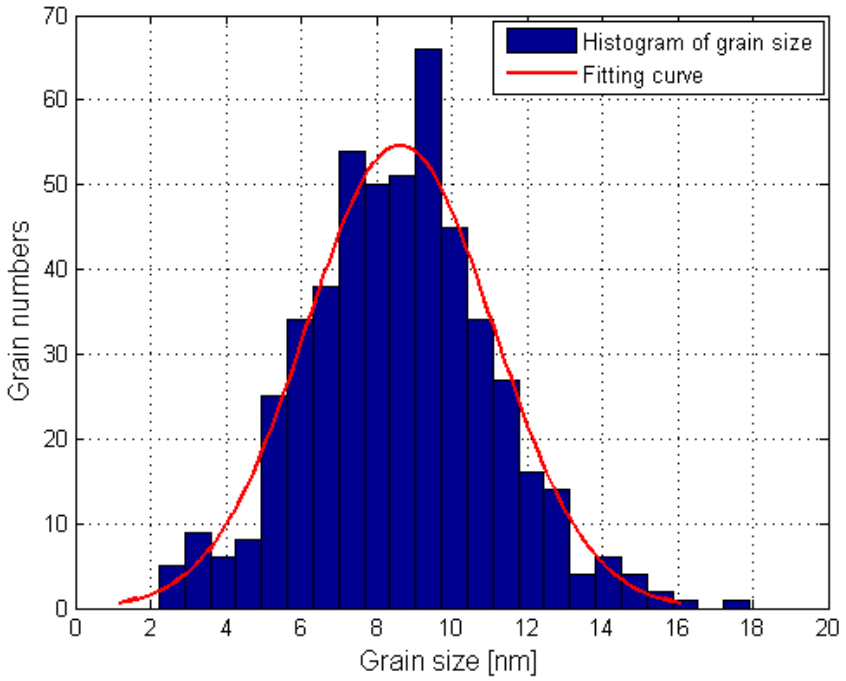


Figure 2.3: An example of grain distribution (500 grains, mean grain size = 8.6 nm, standard deviation = 2.1 nm) generated by Voronoi configuration. A logarithmic normal curve is also showed with solid line.

Figure 2.2 shows an example of an array of 500 planar Voronoi cells. A uniform grain boundary of 1 nm is included between the adjacent grains. For the generation of this array, first random seeds are distributed uniformly within a two-dimensional space. Then a number of vectors have been drawn from a seed to the adjacent seeds. After that, we generate orthogonal lines to the vectors at their mid-

positions. According to the number of adjacent seeds, the total number of orthogonal lines will be determined. Eventually a small enclosed space is formed by connecting the orthogonal lines to the vectors to each other to make polygonal Voronois cell. The polygonal grains which are generated by this procedure are very similar to the growth of real grains. In real grains, random islands are generated by sputtering and the polycrystalline structure is formed after crystals grow along the islands. More detail on sputtering technique will be described in chapter 3. To avoid the edge effect, geometric and magnetic periodic boundary conditions are applied to the array of grains.

Our micromagnetic model includes the parameters to define a recording layer such as average grain diameter $D_{ave}$, standard deviation of diameter $\sigma_D$, space between adjacent grains, and recording layer thickness $\delta$. The variance of grain size and the irregularity of grain shape can be easily changed by adjusting the minimum distance between seed points [2.3]. One example of a grain size distribution with 500 grains is shown in Figure 2.3. The average grain diameter is equal to 8.5 nm and the standard deviation equals 21.5 % of the average grain diameter. A logarithmic fitting curve is also drawn, which is found to be in compliance with the distribution.

## 2.3 Micromagnetic Energy Terms of Grains

In micromagnetic simulations, the micromagnetic grains of a recording layer and the micromagnetic unit cells of the other recording structures such as a write head and a soft underlayer are their own domains that can be modeled with

the LLG equation. The LLG formula can be numerically integrated to predict the magnetization behavior of each domain caused by the applied magnetic field. As mentioned in Chapter 1, the domain structure is a result of minimizing the total free energy, and it represents either a local or an absolute energy minimal state. Without considering magnetoelastic and surface anisotropy effects, the total magnetic energy $E_{tot}$ of a single domain grain subjected to an external field can be expressed as [2.2]:

$$E_{tot} = E_{ms} + E_{ani} + E_{ex} + E_Z \,, \tag{2.3}$$

where $E_{ms}$ is the magnetostatic interaction energy, $E_{ani}$ is the magnetocrystalline anisotropy energy, $E_{ex}$ is the intergranular exchange coupling energy, and $E_Z$ is Zeeman energy. Each energy term is a function of magnetization **M**. The first three energy terms are always present to some extent in a ferromagnet. The last energy term is the response to the applied field, and it defines the magnetization process and hysteresis loop. All energies used in micromagnetic models are taken to produce magnetic fields, which contribute to the effective field in the LLG formula. The effective field of a grain is required during the iterative integration for both dynamic and static (equilibrium state) micromagnetic calculations using the LLG formula. Generally, it is obtained from the energy densities:

$$\mathbf{H}_{eff} = -\frac{\partial E_{tot}}{\partial \mathbf{M}} = -\left(\frac{\partial E_{ms}}{\partial \mathbf{M}} + \frac{\partial E_{ani}}{\partial \mathbf{M}} + \frac{\partial E_{ex}}{\partial \mathbf{M}}\right) + \mathbf{H}_{app} \,, \tag{2.4}$$

where $\mathbf{H}_{app}$ is the applied field. In the following sections, the energy terms in the magnetic grains of the recording media are discussed based on the classical theories

of magnetism. In addition, the transformation of the energy term to an equivalent effective field will be derived.

### 2.3.1 Magnetostatic Energy

The magnetostatic energy is the interaction between the magnetization and the magnetic field. In our system, it arises from the interaction among all the other magnetic grains. As mentioned previously, a magnetized grain generates magnetic field both within the body, called the demagnetization field, and outside the grain, called the stray field. These fields are entirely dependent on the grain geometry and its magnetization state. The total magnetostatic energy in a volume $V$ can be represented by

$$E_{ms} = -\frac{1}{2}\iiint (\mathbf{H}_{ms} \cdot \mathbf{M}) dv \ , \tag{2.5}$$

where $\mathbf{H}_{ms}$ is the magnetostatic interaction field generated by $\mathbf{M}$, and the constant of $\frac{1}{2}$ avoids energy double counting when the energy is summed in the volume. In general, the magnetic field can be calculated either by using Maxwell equations through a scalar potential calculation or from the calculation of magnetostatic interaction energy. The total magnetostatic field can be represented by the integration of magnetic charge over the whole thin recording layer:

$$\mathbf{H}(\mathbf{r}) = -\iiint \left(\nabla \cdot \mathbf{M}(\boldsymbol{r}')\right) \frac{(\boldsymbol{r} - \boldsymbol{r}')}{|\boldsymbol{r} - \boldsymbol{r}'|^3} \boldsymbol{d^3 r}' + \iint (\mathbf{M}(\boldsymbol{r}') \cdot \mathbf{n}) \frac{(\boldsymbol{r} - \boldsymbol{r}')}{|\boldsymbol{r} - \boldsymbol{r}'|^3} \boldsymbol{d^2 r}' \tag{2.6}$$

where $\nabla \cdot \mathbf{M}$ is volume magnetic charge density, $\mathbf{M} \cdot \mathbf{n}$ is surface magnetic charge density, $\boldsymbol{r}$ is the observation point, $\boldsymbol{r}'$ is the location of the source charge and $\mathbf{n}$ is the unit vector normal to the surfaces. In our model, the magnetic moment is

uniform within the layer so the first term on the right hand side is zero. In micromagnetic analysis, almost all computation time has been consumed on the calculation of magnetostatic energy. Moreover, it is difficult to obtain accurate results. For example, the Voronoi grains have polygonal top and bottom surfaces and rectangular side surfaces. The interaction energy between grain *i* and *j* can be calculated over three kinds of surface pair intergrations such as side surface of $i^{th}$ grain to side surface of $j^{th}$ grain, side surface of $i^{th}$ grain to top or bottom surface of $j^{th}$ grain, and top or bottom surface of $i^{th}$ grain to top or bottom surface of $j^{th}$ grain. The computationally easiest way is to pre-calculate a magnetostatic tensor $\overleftrightarrow{T}_{ij}$ from the equation (2.6). The interaction energy tensor between grain *i* and *j* is composed of elements in a matrix form as:

$$\overleftrightarrow{T}_{ij} = \begin{bmatrix} T_{ij}^{xx} & T_{ij}^{xy} & T_{ij}^{xz} \\ T_{ij}^{yx} & T_{ij}^{yy} & T_{ij}^{yz} \\ T_{ij}^{zx} & T_{ij}^{zy} & T_{ij}^{zz} \end{bmatrix} \tag{2.7}$$

It depends on the shape, the geometry of the cell array and the distance to the observation point. Therefore the expression for our application becomes

$$\mathbf{H}_{ms}(\mathbf{r}_i) = \sum_{j=1}^{N} \overleftrightarrow{T}_{ij} \mathbf{M}(\boldsymbol{r}_j) \ . \tag{2.8}$$

In our micromagnetic simulations, only demagnetization fields or the inter interactions between magnetic structures are considered. The computation of the demagnetization matrix for the Voronoi grains is based on the integration of the magnetostatic interaction from triangular or rectangular surfaces (geometric mapping techniques) [2.4]. If we consider a recording layer of two stacks such as exchange coupled composite (ECC) media, magnetostatic demagnetization fields

can be calculated from (2.6). However, this calculation may be monotonous due to the averaging over the entire volume. Another method would be to divide each layer into many small magnetic dipoles. The magnetostatic interaction tensor can be obtained from the energy calculation between all dipoles. The dipole field approximation is given by

$$\mathbf{H}_{dipole} = \frac{3(\mathbf{M} \cdot \hat{n}) \cdot \hat{n} - \mathbf{M}}{R^3} V \tag{2.9}$$

where $R$ is the distance between the observation point and the dipole, V is the volume of the dipole and $\hat{n}$ is the unit vector directed from the dipole to the observation point. This will be a good approximation if the sections representing each dipole are much smaller than the distance between the two layers.

### 2.3.2 Crystalline Anisotropy Energy

In modern magnetic storage applications, the material of the magnetic grains possesses strong uniaxial crystalline anisotropy. The physical origin of the crystalline anisotropy is the spin-orbit interaction of the electrons. Phenomenologically, the energy is related to the local directions of magnetization with respect to the easy axes. This energy results from a hexagonal closed packed (HCP) structure in recording media deposition. The uniaxial crystalline anisotropy energy can be represented by

$$E_{ani} = K_{u0} + K_{u1} sin^2\theta + K_{u2} sin^4\theta + \cdots \tag{2.10}$$

where $K_{u0}$, $K_{u1}$, $K_{u2}$ … are the crystalline anisotropy energy constants, and $\theta$ is the angle between the magnetization and the anisotropy easy axis. If the magnetization is collinear to the easy axis, the anisotropy energy is lowest. Meanwhile, if the

magnetization is orthogonal to the easy axis, the anisotropy energy is highest. For application convenience, the uniaxial anisotropy energy is often simplified as

$$E_{ani} = K_u sin^2\theta = K_u(1 - |\mathbf{k} \cdot \mathbf{m}|^2) \tag{2.11}$$

after neglecting the negligibly small terms higher order terms, where $K_u$ (in erg/cm$^3$) is a dominant term of uniaxial anisotropy constant, and **k** and **m** are easy axis orientation and magnetization, respectively. The effective anisotropy field can be obtained by simply taking the derivative of the energy density with respective to the magnetization vector and multiplying a negative sign. The expression of the effective field of the crystalline anisotropy is

$$\mathbf{H}_{ani} = -\frac{\partial E_{ani}}{\partial \mathbf{M}} = H_k(\mathbf{k} \cdot \mathbf{m})\mathbf{k} \tag{2.12}$$

where $H_k = \frac{2K_u}{M_s}$ is called the anisotropy field. Anisotropy constant is usually measured from experiment. The experimentally measured $K_u$ is an averaged value with grain volume, but in a real magnetic specimen, the magnitude of $K_u$ varies from grain to grain. In my micromagnetic models, the magnitude of anisotropy field is usually taken to be the same in all grains: however, the easy axes of grains can be changed according to a specific angular distribution.

### 2.3.3 Exchange Coupling Energy

Ferromagnets, ferrimagnets, and anti-ferromagnets all have a common characteristic which is known as exchange coupling interaction. Ferromagnetic materials especially have a strong interaction between spins. According to the sign of the spin-spin interaction, each spin has a tendency to align surrounding spins parallel or anti-parallel to its own direction. In quantum mechanics, the interaction

between spins, known as exchange coupling, is a result of the Pauli-exclusion principle. It requires that two electrons too close to each other will have parallel spins. In the Heisenberg Hamiltonian format, the exchange interaction of atoms is represented by

$$E_{ex} = -\sum_{i,j=1}^{M} J_{i,j}\mathbf{S}_i \cdot \mathbf{S}_j \tag{2.13}$$

where $M$ is the number of atoms and $J_{i,j}$ is the exchange integral that includes the overlap of the eigenfunctions of electrons and is typically inversely proportional to the distance between the atoms [2.5]. As the exchange integral value decreases very fast with increasing distance, the exchange interaction is generally considered only for the nearest neighbor spins.

In micromagnetics, the exchange coupling energy between nearest neighbor grains is included based on the quantum mechanical expression. The exchange energy density between these regions can be expressed by

$$E_{ex} = -J\sum \mathbf{M}_i \cdot \mathbf{M}_j \tag{2.14}$$

where $J$ is the exchange constant in erg/cm$^3$. Equation (2.14) measures the strength of the exchange interaction between two magnetized regions. In a Voronoi configuration, the grain boundaries vary with their nearest neighbors, thus different interfacial effects between grains should be considered for exchange energy calculation. If we reasonably assume that the exchange energy between two grains is proportional to their interfacial area, then the total exchange energy density can be modified as

$$E_{ex} = -J \sum \mathbf{M}_i \cdot \mathbf{M}_j \frac{a_{ij}}{a_{ave}} \tag{2.15}$$

where $a_{ij}$ is the interfacial area between grain *i* and *j*, and $a_{ave}$ is average side area if grains were hexagons. It is used to normalize the interfacial area. From equation (2.15), the effective exchange field at grain *i* can be calculated by

$$\mathbf{H}_{ex} = 2J \sum \mathbf{M}_j \frac{a_{ij}}{a_{ave}} . \tag{2.16}$$

Unless there is a thick nonmagnetic boundary to completely decouple the adjacent grains, the lateral inter-granular exchange coupling always exists and should be included in modeling. In the continuum approximation, another exchange energy expression which can be derived from equation (2.13) is represented by

$$E_{ex} = A\left(\left(\frac{\partial m_x}{\partial x}\right)^2 + \left(\frac{\partial m_y}{\partial y}\right)^2 + \left(\frac{\partial m_z}{\partial z}\right)^2\right) \tag{2.17}$$

where $A = \frac{J\mathbf{S}^2}{a}$ is the exchange stiffness constant of the material and $a$ is the lattice parameter of unit cell.

### 2.3.4 Zeeman Energy

The Zeeman energy is the magnetic energy of a magnetic moment under an applied field, $\mathbf{H}_{app}$. It is expressed as

$$E_Z = -\mathbf{M} \cdot \mathbf{H}_{app} \tag{2.18}$$

The maximum Zeeman energy occurs when the applied field is orthogonal to the magnetization and conversely, the minimum energy occurs when the field is aligned with the magnetization.

## 2.4 Thermal Fluctuation Energy

Systems experiences phase transitions owing to random thermal fluctuations. These fluctuations are usually largest close to the phase transition temperature and conversely smaller at lower temperatures. In particular, the magnetic energy stored in a nano-scaled magnetic particle is comparable to the thermal energy. Thus, a nanocrystalline magnetic particle may become superparamagnetic at a blocking temperature. Thermal fluctuation energy approximately equals $k_BT$. Under this energy, the probability, $P(\Delta E)$ of magnetization switching per unit time of a magnetic particle is given as

$$P(\Delta E) = f_0 \tau e^{-\frac{\Delta E}{k_B T}} \tag{2.19}$$

where $\Delta E (= KV)$ is the energy barrier that the magnetization should overcome to switch between two stable states and $f_0$ and $\tau$ are the attempt frequency and the thermal relaxation time respectively. In a real magnetic material, the attempt frequency also depends on many parameters such as a damping constant, temperature, applied field, and so on. Hence, accurate theoretical formulae of the attempt frequency are required for predicting quantitatively the superparamagnetic limit and modeling experiment for applications. Based on equation (2.19), the magnetization switching probability is inverse-exponentially proportional to the ratio of the energy barrier to the thermal fluctuation energy. As this ratio decreases, the switching of magnetization between the stable states is more likely to occur easily. Therefore this thermal fluctuation field becomes part of the effective so that it can be modeled with the Landau-Lifshitz-Gilbert (LLG) equation. The LLG

equation can be modified with the effective thermal fluctuation field. This is called the stochastic LLG equation shown as

$$\frac{d\mathbf{M}}{dt} = \frac{\gamma}{1+\alpha^2}\mathbf{M} \times \left(\mathbf{H}_{eff} + \mathbf{h}(t)\right) - \frac{\alpha\gamma}{(1+\alpha^2)M_s}\mathbf{M} \times \left(\mathbf{M} \times \left(\mathbf{H}_{eff} + \mathbf{h}(t)\right)\right) \tag{2.20}$$

where the thermal fluctuation field is a Gaussian random process with mean equal to zero. The correlation function of the fluctuation field component can be described as

$$\langle h_i(t) h_j(t+\tau)\rangle = \sigma^2 \delta_{ij} \delta(\tau) \tag{2.21}$$

where i, j = 1,2,3, and $\sigma^2 = \frac{2k_B T\alpha}{\gamma M_s V \Delta t}$ . The Dirac $\delta$ function indicates that the autocorrelation time of the fluctuation field is much shorter than the rotational response time of the system, while the Kronecker $\delta$ function represents the assumption that the different components of the fluctuation field are not correlated with each other. In addition, it is assumed that the fluctuation fields acting on different magnetic moments are independent. Equation (2.20) is solved by using the forth order Runge-Kutta method and a uniform random number generator has been used to obtain the thermal fluctuation fields.

# Chapter 3 Magnetic Nanoparticles for Hyperthermia Cancer Treatment

Great attention has been paid to nanotechnology in medicine from long time ago. The concept of nanotechnology was first coined by Richard Feynman in 1959 in his lecture "There's plenty of room at the bottom". Since 1998, both nanotechnology and bio-technology are very rapidly advancing research fields. Many opportunities exist for the design of new medical therapeutic techniques and instrumentation using these technologies. Magnetic nanomaterials can be very useful for many biomedical applications.

In chapter three and four, a brief motivation and background for this study will be expressed and the fundamental concept of using ferromagnetic nanoparticles for hyperthermia cancer treatment will be described. Also, the characteristics and the preparation method of magnetic nanoparticles will be presented shortly. Based on the important concepts of magnetic nanoparticles, the optimization technique of magnetic anisotropy and applied fields for hyperthermia will be presented.

## 3.1 Introduction

Magnetic nanoparticles have great potential in the biomedical area, such as drug delivery, magnetic resonance imaging (MRI), and magnetic hyperthermia. The nanometer size scale helps enable control of particles in the human body. The large

surface to volume ratio at this range is also beneficial for promoting biological reactions through contact. Interest in the application of nanoparticles has increased in recent years. Magnetic hyperthermia, which utilizes the magnetic property and small size of particles simultaneously to help cure cancer [3.1], is one of the most attractive topics among those.

A great advantage of hyperthermia treatment is the possibility to generate localized heat and kill malignant tumor cells selectively. The underlying principle is the higher sensitivity of tumor cells to temperature [3.1]. Sensitivity to heat derives from a lack of oxygen in tumor cells because of the poor blood flow there. In approximately 41ºC - 46ºC range [3.1], viability of tumor cells will be greatly reduced while healthy cells are hardly affected.

Superparamagnetic particles are generally used in hyperthermia, among which magnetite is one of the most widely studied due to its biocompatibility and magnetic properties [3.2]. An AC field is applied to a particle solution during the heating process. Dissipation of heat is based on Néel and Brownian relaxation [3.1]. Néel relaxation is due to the magnetization rotation inside the nano-crystals with respect to the crystal axis. An alternating field will induce fluctuations and realignment of the moment which generates heat. Brownian relaxation is from the rotation of the whole particle in solution where friction causes release of heat. There has been research on the contribution of these two mechanisms in total energy dissipation for different materials, particle size and solvents. The Néel relaxation mechanism can be considered to be hysteresis loss [3.4]. It is well known that ferromagnetic materials have hysteresis behavior when subjected to magnetic field. The area of a hysteresis loop represents energy loss per unit volume which

can be expressed by $\oint \mathrm{H}(t)dB$ [3.2]. If ferromagnetic particles with uniaxial anisotropy can be used under a large enough field, hysteresis loss will be promising [3.2].

More attention has been paid to high magnetic moment materials other than iron oxides recently. Theoretically, specific loss power is proportional to the square of the moment[7]. The low moment of iron oxide particles prevent them from becoming highly efficient materials in hyperthermia (so that reduced dosage can be used on patients [3.7].) Therefore, high moment and biocompatible nanoparticles are needed. Experimental data has proven the efficiency of high moment nanoparticles compared to iron oxides [3.2]. Surface modified $Fe_{70}Co_{30}$ nanoparticles with approximately 226 emu/g magnetization, more than 2 times higher than magnetites [3.6], are studied in this chapter as one of the potential candidates for hyperthermia.

## 3.2 Experiment

### 3.2.1 Preparation of FeCo nanoparticles

Self-assembled nanoparticles are playing an important role in modern magnetic material science. Our collaborations (Ying, Jian-Ping, etc.) prepared TEM $Fe_{70}Co_{30}$ nanoparticles by a unique physical gas condensation system [3.2]. Figure 3.1 shows the schematic of physical gas condensation equipment. FeCo alloy target with atomic composition 70:30 was used as the sputtering source. $Ar_2$ gas was provided as both sputtering gas and carrier gas. During deposition, gas pressure was kept within 400mTorr to 600mTorr range. In order to do surface modification

and make biocompatible solution in future, particles were deposited on PVP (Polyvinylpyrrolidone) pre-coated glass slides.

Modification of the magnetic field on the target surface was done in order to get uniformly distributed cubic FeCo particles [3.2]. The surface field at the target was designed to reach a certain value so that sufficient glow discharge density was maintained, which was critical for the good crystallinity. In addition, a narrow size distribution was achieved by keeping sputtering voltage almost constant, an indicator of stable glow discharge [3.11].

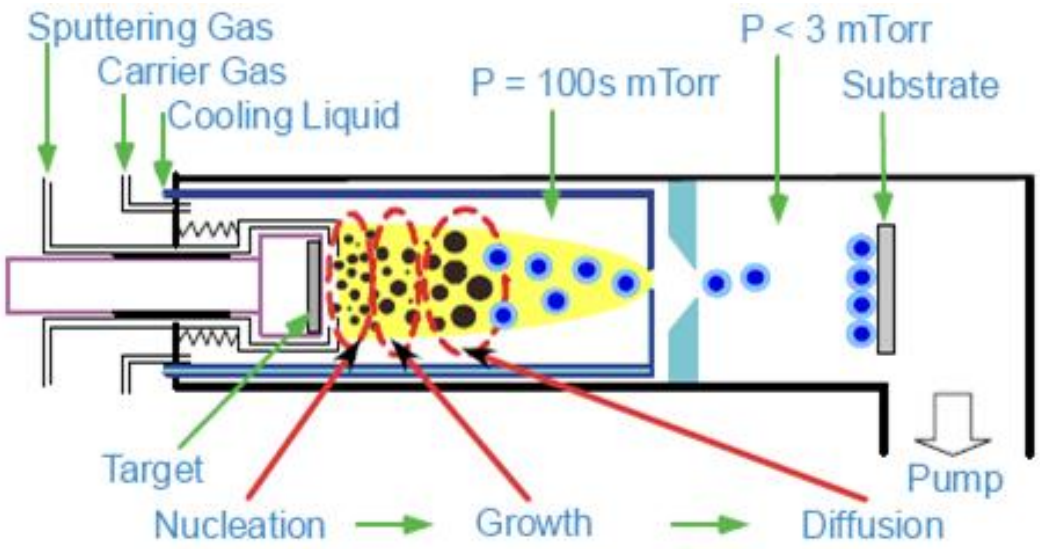


Figure 3.1: Synthesized method: Schematic of physical gas condensation equipment [3.10]

### 3.2.2 Structural Properties

Our collaborations characterized the morphology and crystal structure of direct deposited FeCo particles by transmission electron microscopy (TEM). Fig 3.2(a) shows the bright field image under low magnification [3.14]. Plane view of

particles is dominantly cubic shape while it's not very clear about exact 3D dimension view. So particles are assumed to be similar with cubes. A size distribution chart (Fig 3.2 (b)) presents a small size distribution [3.14]. Particle mean size is 12nm with 13.6% standard deviation. A higher magnification bright field image is shown in Fig 3.3 (a). Because particles were kept in ambient air, about 2nm thick oxidation layer is estimated based on the contrast in the TEM image. Selected area diffraction pattern (Fig 3.3 (b)) shows a body-centered-cubic crystal structure. Good crystal growth is implied by the cubic morphology and strong diffraction.

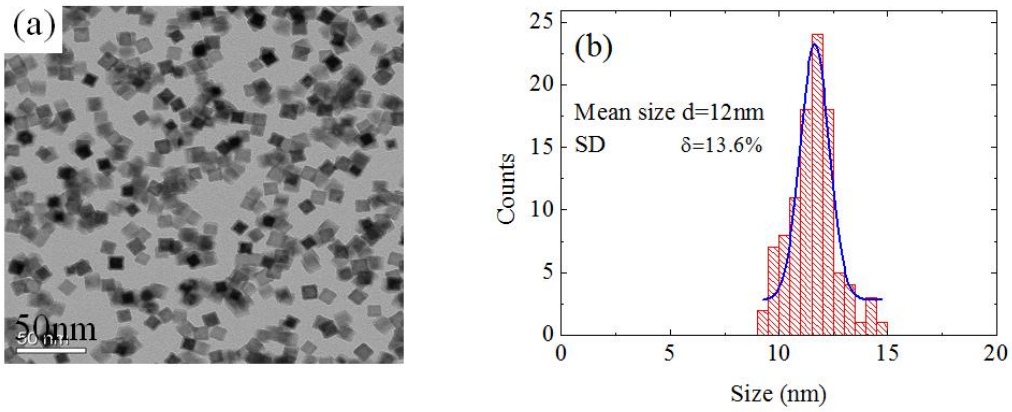


Figure 3.2: (a) Bright field image of FeCo nanoparticles at low magnification (b) Size distribution of FeCo nanoparticles [3.14]

The magnetic properties of the FeCo nanoparticles were analyzed by alternating field gradient magnetometer (AGM) at room temperature. A hysteresis loop with 82Oe coercivity is shown in Fig 3.4 [3.14]. This served as one of the micromagnetic simulation cases.

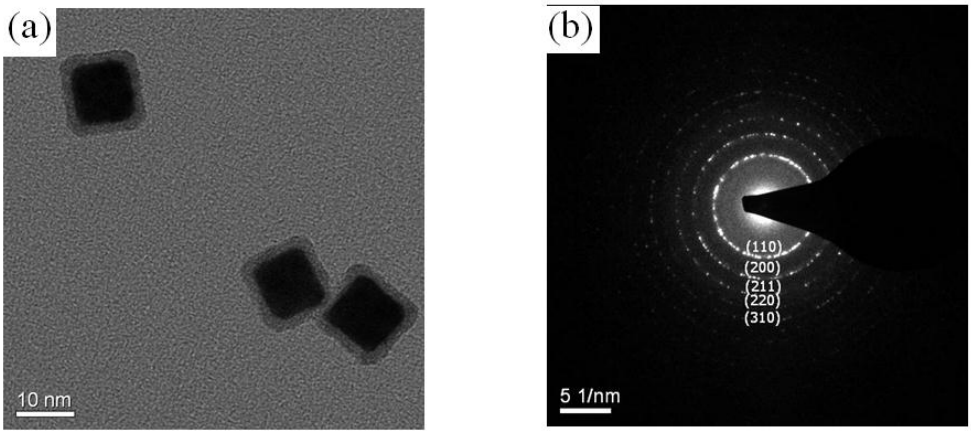


Figure 3.3: (a) Bright field image of FeCo nanoparticles at high magnification (b) Selected area diffraction [3.14]

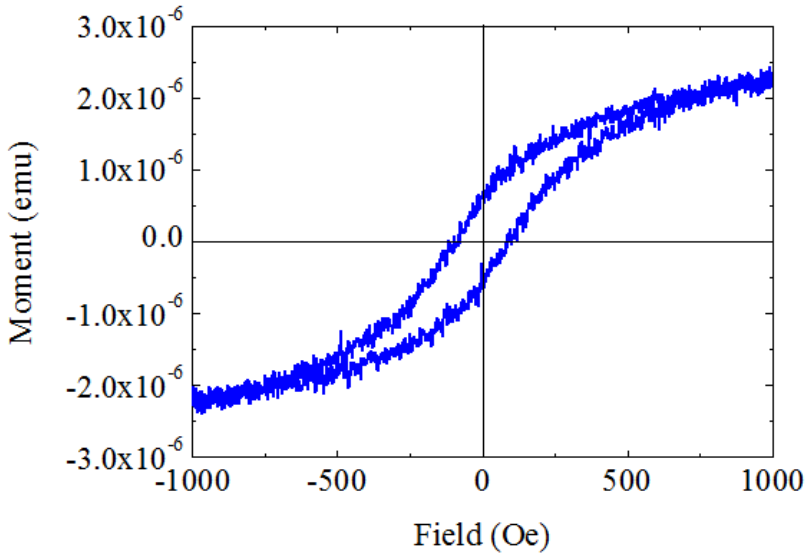


Figure 3.4: Hysteresis loop measured by AGM [3.14]

# 3.3 Micromagnetic Simulation Method

## 3.3.1 Thermal Micromagnetic Model

As denoted in the previous chapter, our model for this study is based on the numerical integration of the stochastic Landau-Lifshitz-Gilbert (LLG) equation (2.20). The effective field acting on the magnetization includes the magnetocrystalline anisotropy field, the applied field, the magnetostatic field and the thermal fluctuation field [3.12]. A scaling relationship between measurement time and thermal field has been used in our simulation to reduce computational time [3.13]. We assume that the FeCo nanoparticles are magnetized uniformly: therefore, a single magnetization vector is assigned to each particle. For cubic FeCo particles, the magnetocrystalline anisotropy is given

$$E_K = K_1(\alpha_1^2\alpha_2^2 + \alpha_2^2\alpha_3^2 + \alpha_3^2\alpha_1^2)V, \tag{3.1}$$

where $K_1$ is the anisotropy constant and $\alpha_1$, $\alpha_2$, and $\alpha_3$ are the direction cosines of the magnetizations. A uniaxial shape anisotropy can be written

$$E_{uni} = K_{uni}Vsin^2(\theta), \tag{3.2}$$

where $K_{uni}$ is the uniaxial anisotropy constant, and $\theta$ is the angle to the easy axis. We include magnetostatic interactions by treating each particle as a single dipole.

## 3.3.2 Magnetic Properties using a Fitted Method

Hysteresis loops were calculated for two experimentally measured sweep frequencies: $2.79 \times 10^{-4}$ Hz and 0.13 Hz. Both particle volume and anisotropy constant were varied to match the experimental results. Assuming only cubic anisotropy, we found an optimized volume of 520 $nm^3$ and optimized anisotropy of

$5.8 \times 10^6$ ergs/cm$^3$ [3.14]. This volume corresponds to a cube that is 8 nm along each edge. This would be the volume obtained if the experimental 12 nm cubes included a 2 nm nonmagnetic shell, which appears likely. The anisotropy is higher than that found in bulk materials. This suggests that the dominant anisotropy is a uniaxial shape anisotropy or surface anisotropy. Figure 3.5 shows the predicted hysteresis loop for 0.13 Hz, optimized uniaxial anisotropy of $1.3 \times 10^6$ ergs/cm$^3$, and the same optimized volume of 520 nm$^3$ [3.14]. This corresponds to a shape contribution caused by one axis exceeding the length of the other axis by 1nm. This kind of imperfection seems likely and probably caused most of the anisotropy.

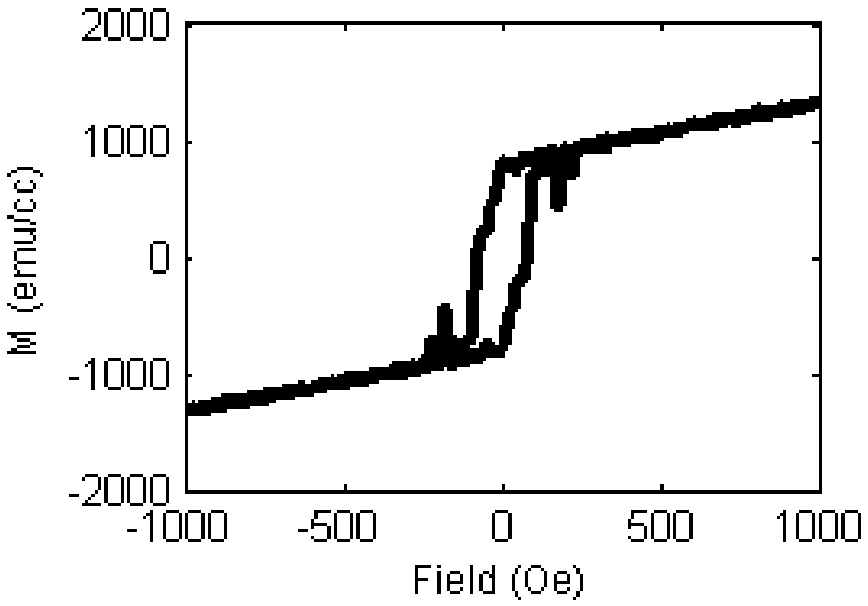


Figure 3.5: Hysteresis loop of randomly oriented sample swept at a frequency of 0.13 Hz. All particles have volume in 520 nm$^3$ and a uniaxial anisotropy constant $1.3 \times 10^6$ ergs/cm$^3$. The spikes are a consequence of thermal fluctuation in the limited theoretical sample [3.14]

## 3.4 Summary

High moment $Fe_{70}Co_{30}$ nanoparticles with a 12 nm mean size and a narrow size distribution were simulated. Micromagnetic simulation was performed to calculate hysteresis loops for different experimentally measured sweep frequencies. Simulation results suggested cubic particles with 8nm edge length, which is consistent with experiment considering the oxide layer. The anisotropy appears to be dominated by a uniaxial term with an optimized value of $1.3 \times 10^6$ ergs/cm$^3$. It is suspected to come from non-uniform oxidation which introduces a shape contribution.

# Chapter 4 Optimization of Magnetic Anisotropy and Applied Fields for Hyperthermia

## 4.1 Introduction

Magnetic nanocrystalline particles in alternating magnetic fields may have great heating efficiencies caused by hysteresis losses from the magnetization reversal processes. The specific loss power (SLP) of magnetic nanoparticles depends on magnetic moment, anisotropy energy density, particle size, and size distribution [4.1]. Among those components, SLP is strongly dependent on magnetic moment and anisotropy constant. In this chapter, the interesting region where the thermal energies and the energy barriers are comparable has been explored through numerical micromagnetics and explained analytically.

## 4.2 Relaxation Mechanisms

There are two different source of energy loss. Néel relaxation occurs due to the reorientation of the magnetic moment inside of the particles. The characteristic relaxation time is given by

$$\tau_N = \tau_0 e^{(KV/k_B T)}, \tag{4.1}$$

where $\tau_0$ is thought to be $10^{-9}$ s [4.8], $K$ is an anisotropy constant, and $V$ is the volume of particle. The equation shows the relaxation time depends on the ratio of the anisotropy energy to the thermal energy. The hysteresis loss power may be easily estimated from the measured hysteresis loop. The comparison between estimated values of hysteresis loss power and results of calorimetric determination of the heat power has been made and shown to be in good agreement [4.2]. The other source of energy loss is caused by the reorientation of the whole particle itself in a fluid solution of magnetic nanoparticles (Brown relaxation). In general, the two different relaxation mechanisms occur at the same time and an effective characteristic time is given by

$$\tau_{eff} = \frac{\tau_N \tau_B}{\tau_N + \tau_B}, \tag{4.2}$$

where $\tau_B$ is the Brown relaxation. In an alternating magnetic field the frequency response of the magnetic nanoparticles can be investigated by measuring susceptibility spectra. Susceptibility is composed of real and imaginary parts. Magnetic loss is related to the imaginary part of susceptibility $\chi^{"}$ which is described by

$$\chi^{"} = \chi_0 \frac{\omega\tau}{1 + (\omega\tau)^2}, \tag{4.3}$$

where $\chi_0 = \frac{M_S^2 V}{a k_B T}$ is the static susceptibility, $M_S$ is saturation magnetization, and $a$ is a factor depending on the ratio of the anisotropy energy to thermal energy in the range of 1-3 [4.4]. The loss power density in alternating magnetic field is proportional to magnetic field amplitude, field frequency, and $\chi^{"}$. It is expressed by

$$P = \frac{H^2 \omega \chi''}{2} . \quad (4.4)$$

As the loss power density increases, the heating generation increases as well. Increasing magnetic field amplitude and frequency is the easiest way to raise the loss power density. However, magnetic hyperthermia has physical limits for biocompatibility such as maximum RF-magnetic field amplitudes and frequency. Brezovich has discussed the upper limit of the product between magnetic field amplitude and frequency [4.5]. Magnetic losses of different magnetic nanoparticles show a variety of nonlinear dependences on field amplitude, field frequency, and volume etc. Therefore high magnetic moment nanoparticles such as iron cobalt with gold coating are very promising for hyperthermia application. Their performance will be optimized using micromagnetics to determine Néel relaxation by integrating minor hysteresis loops.

## 4.3 Micromagnetic Simulation Method

### 4.3.1 Thermal Micromagnetic Model

Micromagnetics allows prediction for Néel relaxation loss while avoiding the oversimplification inherent to analytic theories that can produce erroneous answers or miss important discoveries. The simulation was based on the numerical integration of the stochastic Landau-Lifshitz-Gilbert (LLG) using the thermal fluctuation formalism developed by Brown [4.6]. The iron cobalt nanoparticles are assumed uniformly magnetized. A uniaxal shape anisotropy energy is dominant and given by the equation (3.2). The volume of each grain is 520 $nm^3$ [4.11]. The

calculation included magnetostatic interactions between 10 particles with random easy axes and was repeated 1000 times to generate adequate statistics.

### 4.3.2 Attempt Frequency

The Attempt frequency of magnetization comes from the mean rate of transition between orientations. The mean rate of transition $r_{ij}$ is described by

$$r_{ij} = c_{ij} e^{-(V_m - V_i)v/k_B T}, \tag{4.5}$$

where $c_{ij}$ is the attempt frequency of magnetization, in other words probability per unit time of jumping to the different orientations [4.6]. $V_m$ and $V_i$ are maximum energy at specific angle and two different minimum energies at different angles, respectively. The attempt frequency can be described as

$$c_{ij} = \frac{\gamma_0^2 \eta M_s}{1 + (\gamma_0^2 \eta M_s)^2} \sqrt{\frac{v H_c^3 M_s}{2\pi k_B}} (1 - h^2)(1 + h), \tag{4.6}$$

where $\gamma_0$ is gyromagnetic ratio, $\eta$ is dissipation constant, $v$ is volume of the particle, and $h(= H/H_c)$ is magnetic field normalized by coercivity [4.6]. Numerical estimates of the attempt frequency are analyzed in comparison with theoretical predictions from the Fokker-Planck equation for the Neel-Brown model. This equation can be used for high energy barrier approximation, which is the energy barrier $(V_m - V_i)v$ is larger than thermal energy ($k_B T$). For iron cobalt nanoparticles, we obtained approximately $10^7$ [Hz] which is two-order lower than usual attempt frequency [4.10].

## 4.4 Minor Hysteresis Loops

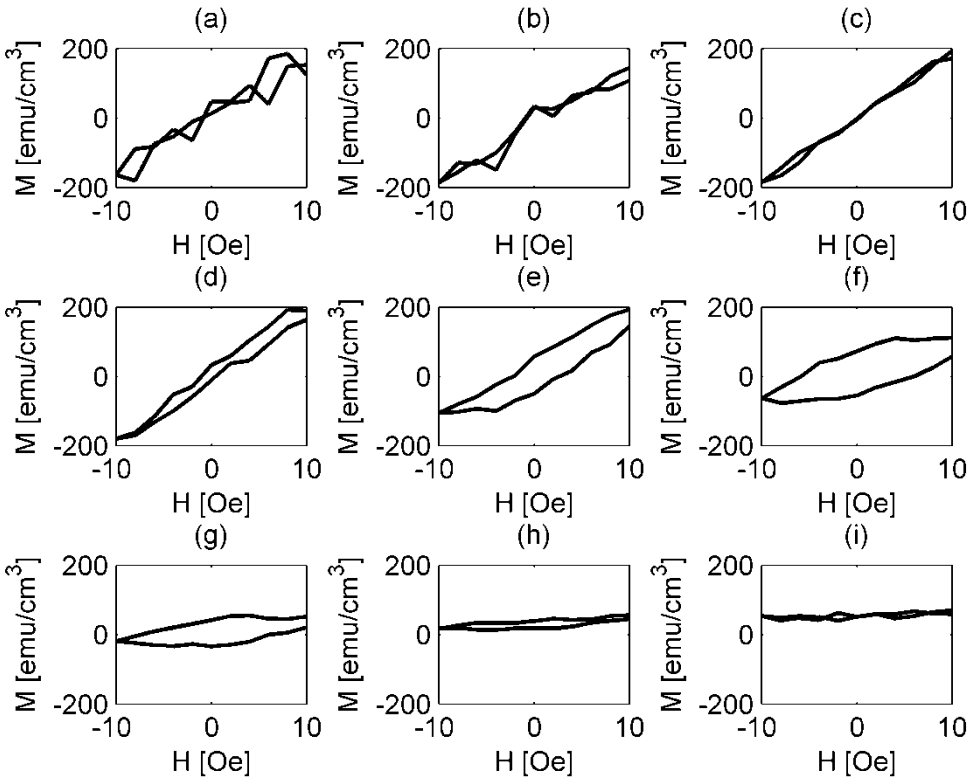


Figure 4.1: Minor hysteresis loops of randomly oriented iron cobalt nanoparticles for different anisotropy energy densities, $K_u$ (ergs/cm$^3$) which are (a) $1\times10^5$, (b) $2\times10^5$, (c) $3\times10^5$, (d) $4\times10^5$, (e) $5\times10^5$, (f) $6\times10^5$, (g) $7\times10^5$, (h) $8\times10^5$, and (i) $9\times10^5$, first published in reference [4.10].

Figure 4.1 shows a variety of minor hysteresis loops evaluated at constant sweep rate for different anisotropy energy densities, $K_u$ [4.10]. In the case of hysteresis loops with small anisotropy constants, superparamagnetic effects are shown in Fig. 4.1 (a), (b) and (c). With increasing anisotropy energy densities, the area of a hysteresis loop increases as shown in Fig. 4.1 (e), (f) and (g). Eventually,

the anisotropy becomes too large for thermal switching, and the loop reverts to a straight line as shown in Fig. 4.1 (h) and (i). Interestingly, we find the attempt frequency $A$ to be about $2 \times 10^7$ Hz [4.10]. This agrees well with reference [4.3], but contradicts the usual assumption of $1/\tau_0 = 10^9$ Hz [4.8].

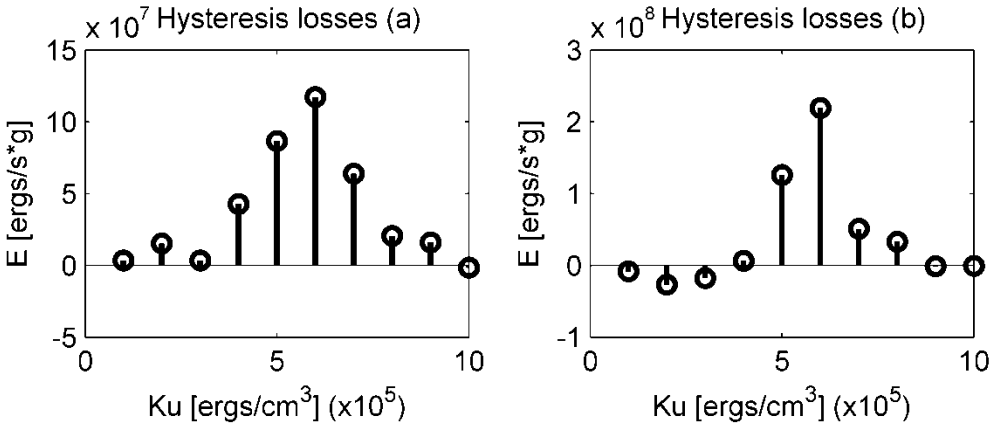


Figure 4.2: Hysteresis losses of randomly oriented iron cobalt nanoparticles for different anisotropy energy densities, $K_u$ from $1\times10^5$ to $1\times10^6$ ergs/cm$^3$, and alternating magnetic field range from -10 to 10 Oe (a) without the static field and (b) with the static magnetic field [4.10].

Figure 4.2 (a) shows the total energy loss for different anisotropy constants for the case of a small oscillating field with magnitude 10 Oe. The energy loss per unit volume can be obtained from $\oint \mathrm{H}(t)dM$ [4.7]. The highest peak shows approximately $120\times10^6$ ergs/(s*g) (equal to 12 W/g) hysteresis loss energy at the anisotropy of $6\times10^5$ ergs/cm$^3$.

## 4.5 Perpendicular Static Fields

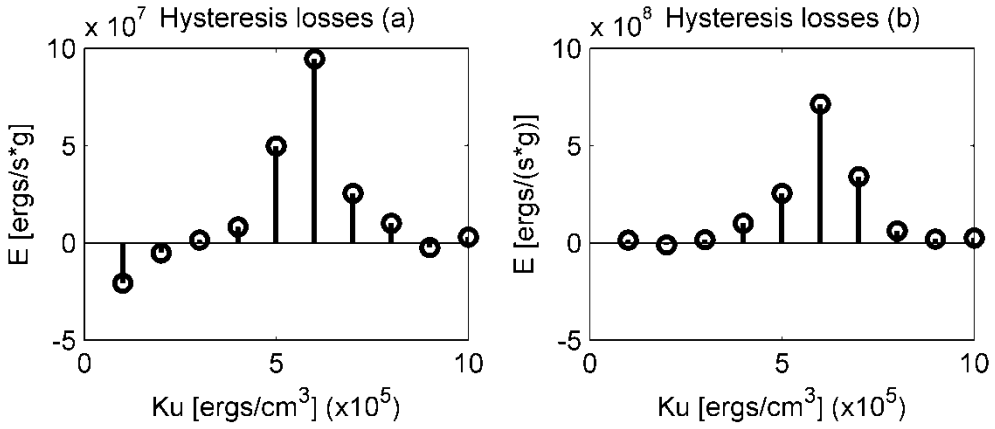


Figure 4.3: Hysteresis losses of randomly oriented iron cobalt nanoparticles for different anisotropy energy densities, $K_u$ from $1\times10^5$ to $1\times10^6$ ergs/cm$^3$, and alternating magnetic field range (a) from -5 to 5 Oe and (b) from -20 to 20 Oe with the static magnetic field respectively [4.10].

We have explored the effects of varying the applied field and find that the combination of a relatively small static field applied perpendicular to the oscillating field approximately doubles the energy loss for a given applied power [4.10]. This is an important benefit for magnetic hyperthermia. Figure 4.2 (b) shows the total energy loss with a 20 Oe static applied field and alternating magnetic field ranging from -10 to 10 Oe for different anisotropy constants. The highest peak shows approximately $220\times10^6$ ergs/(s*g) per particle at the same anisotropy energy density. Similar results are shown in figure 3 (a) and (b) under two different alternating magnetic field ranges. Figure 4.3 (a) shows the total energy per unit volume with a 15 Oe static applied field and alternating magnetic field ranging

from -5 to 5 Oe and figure 4.3 (b) shows the total energy per unit volume with a 25 Oe static applied field and alternating magnetic field ranging from -20 to 20 Oe. The highest peaks show approximately $94\times10^6$ ergs/(s*g) and $710\times10^6$ ergs/(s*g) per particle at the same anisotropy energy density respectively. However, for large oscillating fields, the contribution of the static applied field become much less. For example, the contribution of the static field when the oscillating field is greater than 50 Oe is less than a 10 % increase in loss power for this size particle.

## 4.6 Analytic Expression for Specific Loss Power

### 4.6.1 Power Dissipation by AC Bias of Magnetic Field

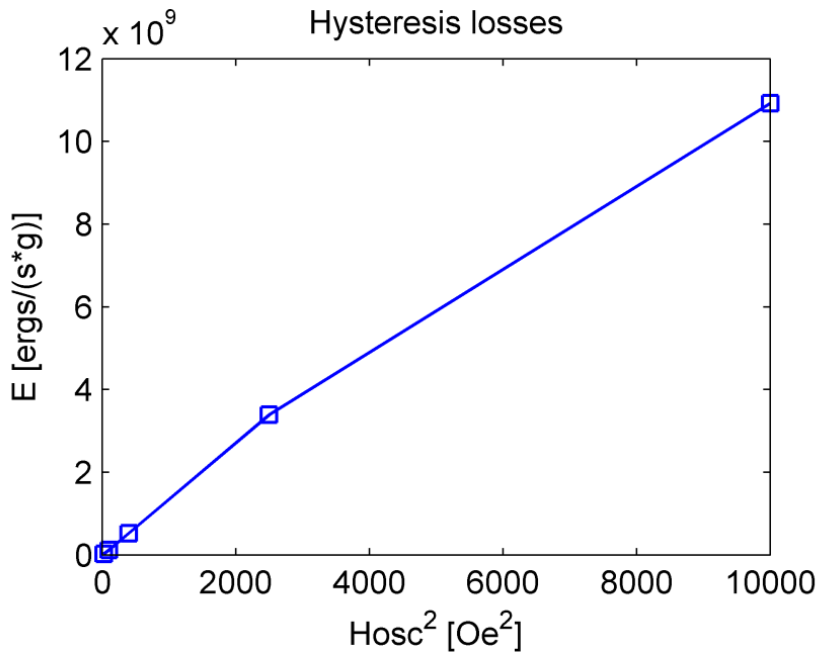


Figure 4.4: Hysteresis losses of randomly oriented iron cobalt nanoparticles vs. $H_{osc}^{\ 2}$ at zero static field [4.10].

The total energy density of a nanoparticle is given by

$$E_{tot} = Ksin^2(\theta) - HM_s\cos(\theta - \psi), \tag{4.7}$$

where $K$ is anisotropy energy density, $\psi$ represents the angle between the easy axis and the magnetic field and $\theta$ represents the angle between the magnetization and the anisotropy axis. For randomly oriented easy axes of the particles, an energy barrier $\Delta E$ can be analytically obtained for the case of $H$ small compared to $2K/M_s$ :

$$\frac{dE}{dsin(\theta)} = 0, \qquad \rightarrow \quad sin(\theta) \approx \frac{HM_s \sin(\psi)}{2K} \tag{4.8}$$

$$E_{min} = \pm HM_s\cos(\psi), \tag{4.9}$$

$$\frac{dE}{dcos(\theta)} = 0, \qquad \rightarrow \quad cos(\theta) \approx \frac{-HM_s \cos(\psi)}{2K} \tag{4.10}$$

$$E_{max} = K - HM_s|sin(\psi)|, \tag{4.11}$$

$$\Delta E = K - HM_s|\sin(\psi)| \pm HM_s \cos(\psi). \tag{4.12}$$

The magnetization direction of each particle can be seen to align with the easy axis for very small field. The magnetization reversal process takes place by transition over this energy barrier. The switching probability is determined by the relation between measuring time and relaxation time. For sufficiently large barrier, the loss power from the energy barrier distribution is given by

$$P = 4AHM_s \cos(\psi)\, sinh\left(\frac{VHM_s\cos(\psi)}{k_BT}\right) e^{-\frac{[K - HM_s|\sin(\psi)|]V}{k_BT}}. \tag{4.13}$$

This expression substantially differs from the usual linear theory as described in the introduction. However, if $VHM_s/(k_BT)$ is not too large, then the loss power can be approximated by

$$P = \frac{4AV(HM_s)^2}{k_BT}\cos^2(\psi)e^{-\frac{KV}{k_BT}} \tag{4.14}$$

which resembles the usual linear expression at optimal (and high) frequencies.

The linear expression is tested in figure 4, which shows the hysteresis losses versus the square of the oscillating magnetic field at a zero static field. It can be seen that for low fields below about 50 Oe, the loss depends linearly on $H_{osc}^2$. This corresponds to $HVM_s \sim\leq k_BT$ which makes sense in view of a hyperbolic sinusoidal function and provides an upper limit to the linear theory.

### 4.6.2 Power Dissipation by AC & DC Bias of Magnetic Field

Under AC bias of magnetic field, the magnetic crystalline nanoparticles generate appreciable heating effect caused by relaxation loss and eddy current loss mechanisms. Eddy current heating is assumed to be negligible due to the small size of the particles. From the relaxation mechanisms, the general expression of specific loss power (SLP) in a suspension of nanoparticles has been derived in [4.9]. According to the SLP, the final goal which increasing power dissipation is easily accomplished by applying large AC magnetic field, frequency and other values of the components in the general expression. However, for biocompatibility, physical limits do not permit use of large applied magnetic field and it's frequency in order to boost specific loss power.

The total energy density of a magnetic crystalline nanoparticle is able to be defined by the equation (4.7). From the total energy density considering only oscillating applied field, an energy barrier and the power dissipation relationships based on rotational relaxation of a nanoparticle have been derived in [4.10]. The derived expression showed the linear relationship between loss power and oscillating field square which is the same as the general equation of SLP.

In this section, the analytical relationships including the static applied field perpendicular to the oscillating applied field as well as the oscillating applied field have been derived. The power dissipation can be obtained by the product of the energy difference and the switching probability over the time coming from the mean rate of the transition between magnetization orientations. From the total energy density, the energy differences are given by

$$dE_1 = 2M_s\left(\overrightarrow{H_{st}} + \overrightarrow{H_{osc}}\right) \cdot \widehat{K}\,, \tag{4.15}$$

$$dE_2 = 2M_s\left(\overrightarrow{H_{st}} - \overrightarrow{H_{osc}}\right) \cdot \widehat{K}\,, \tag{4.16}$$

where $\overrightarrow{H_{st}}$ and $\overrightarrow{H_{osc}}$ stand for static applied field and oscillating applied field respectively and $\widehat{K}$ shows the unit vector of anisotropy of a nanoparticle. We assumed that $\widehat{K}$ is in parallel with $\hat{z}$ axis. Therefore, $\mathrm{dE}_1$ and $\mathrm{dE}_2$ represent energy losses in the first half and the second half of a hysteresis loop. Each power dissipation can be obtained from the derivations of the energy losses and shown by

$$P_1 = \frac{4{M_s}^2 AV}{k_B T}\left[\left(\overrightarrow{H_{st}} + \overrightarrow{H_{osc}}\right) \cdot \widehat{K}\right]^2 e^{-\frac{KV}{k_B T}}\,, \tag{4.17}$$

$$P_2 = \frac{4{M_s}^2 AV}{k_B T}\left[\left(\overrightarrow{H_{st}} - \overrightarrow{H_{osc}}\right) \cdot \widehat{K}\right]^2 e^{-\frac{KV}{k_B T}}\,, \tag{4.18}$$

where $A$ represents an attempt frequency, $V$ is the volume of a nanoparticle and $K$ shows an anisotropy constant. From these two derived equations, the total power dissipation can be approximated by

$$P_{tot} = \frac{4M^2AV}{k_BT}\left\{{H_{st}}^2 \sin^2\theta + 2{H_{osc}}^2 \cos^2\theta\right\}e^{-\frac{KV}{k_BT}}. \quad (4.19)$$

This dissipation relationship based on energy barrier is similar with the general power loss expression and also proves that the combination of a comparatively small static field depending on the amount of oscillating field proliferate the energy loss for a given applied power. Consequently, the angle between the AC bias of magnetic field and the anisotropy direction does not influence to the total power dissipation under the condition of the small range of oscillating applied magnetic fields.

## 4.7 Summary

We have micromagnetically simulated the Néel relaxation of superparamagnetic nanoparticles subject to an oscillating field. We calculate the optimized anisotropy energy of the simulated nanocrystalline iron cobalt particles to be $3.142\times10^{-13}$ ergs which corresponds to an energy barrier of $7.6k_BT$ at room temperature. We find that application of a small field enhances the loss without the necessity for enhanced radiation. The expressions for the advantageous effects of an oscillating field as well as a static field have been derived. The calculation results suggest that the addition of a static field perpendicular to the sinusoidal oscillating applied field would be required for experimental measurement of the

heating power. The frequency of magnetization attempts to surmount the energy barrier is shown to be about two orders of magnitude smaller than previously estimated. Finally, we establish upper limits for the applied field magnitude, beyond which the normal linear theory will fail.

# Chapter 5 Recording Comparison of ECC versus Conventional Media

## 5.1 Introduction

Conventional perpendicular magnetic recording also confronts the superparamagnetic limit and low writability as aid longitudinal magnetic recording, despite the superior recording fields from the combination of a perpendicular head and a soft underlayer. In the mid-2000s, exchange coupled composite (ECC) media was proposed for high areal density recording [5.1] because it allowed smaller grains while retaining adequate thermal stability. Secondary advantages included nucleation of switching near the recording head where gradient was strongest and improved angular dependence of switching field to resist thermal fluctuations. The requisite hard layer and small grain size necessary to fully exploit this idea has proven hard to experimentally develop. Consequently, early commercial production has used “soft” ECC media with reduced ratio of hard to soft anisotropy and grain size unimproved relative to conventional perpendicular media. Nonetheless, it has been experimentally observed that ECC media [5.2], [5.3] can offer superior jitter and transition shape relative to conventional perpendicular media even at this similar grain size.

In this chapter, we show that this effect is reproducible within micromagnetic simulation that includes thermal fluctuations [5.4]. The micromagnetic simulation method is described as well as the simulation model is

depicted in section 5.2. Section 5.3 provides simulation results for optimal anisotropies, transition noise, and transition shape for ECC and conventional media. Additionally in section 5.4, the transition shifts of each media have been analyzed by using eye diagrams.

## 5.2 Micromagnetic Recording Model

In order to explore the deviation of the transition locations and shapes as well as determine the optimal anisotropies for ECC and conventional perpendicular media, micromagnetic simulation based on the stochastic Landau-Lifshitz-Gilbert (LLG) equation using the thermal fluctuation formalism has been carried out. An effective field combines the deterministic uniaxial anisotropy field, the applied field, the magnetostatic field, the exchange field and the thermal fluctuation field. The most intensive computation is to obtain the magnetostatic interaction field for the media grains and the soft materials from the recording head and the soft underlayer. The soft material in the pole tip (write pole plus trailing shield) is discretized into uniform cubic cells in order to calculate the magnetostatic tensor. A geometric mapping technique [5.5] has been utilized to calculate the magnetostatic interaction between grains within the media, as well as the interaction between media grains and soft material cubic cells. The damping constant $\alpha$ was chosen to be 0.2. The LLG equation was solved using the $4^{th}$-order Runge-Kutta method. In this simulation, a time step of $5\times10^{-13}$ s was employed.

### 5.2.1 Conventional & ECC Media Design

We generated practically feasible ECC media with moderate anisotropy ratio between soft and hard layers, and also conventional media, for jitter and transition shape comparisons. Both of them have been generated by using a realistic grain configuration that is composed of planar Voronoi cells at equal average grain size. For the ECC media, the grain model is composed of two parts representing magnetically soft and hard regions. The grain shape of the top part is the same as that of the bottom part except for the different thicknesses. Each part is assumed to be a single domain having uniaxial anisotropy.

Both conventional perpendicular media and ECC media were taken to have a thickness of 15 nm. The non-magnetic grain boundaries are 1 nm. The easy axis dispersion of the grains follows a Gaussian distribution with a standard deviation of 2° and the average grain diameter is 8.6 nm with a standard deviation of 26 %. The intergranular exchange coupling energy is expressed as $E_{ex}$=-$J\mathbf{M}_1\cdot\mathbf{M}_2$ and it is assumed that the exchange energy is proportional to the surface area between the two neighboring grains. We chose a typical intergranular exchange coupling constant of 0.5 to prevent excessive bit decays at low density. All the saturation magnetizations of hard and soft elements of ECC media grains and conventional media grains were set at 600 emu/cm$^3$. This yields a film magnetization of 460 emu/cm$^3$. A moderate anisotropy ratio of 3 between hard and soft elements has been chosen, in accordance with experiment. The total energy of the composite grain [5.1] can be expressed as

$$E_t = -J_{ex}\cos(\theta_2-\theta_1) + K_2\sin^2\theta_2\cdot V_2 + K_1\cos^2\theta_1\cdot V_1 + M_2H\cos\theta_2\cdot V_2 + M_1H\cos\theta_1\cdot V_1 \quad (5.1)$$

where $M_1$ and $M_2$ are the saturation magnetizations of the top and bottom region. $\theta_1$ and $\theta_2$ are the angles between $M_1$, $M_2$ and the applied field $H$. $V_1$ and $V_2$ are volumes of the two regions and $J_{ex}$ is the exchange constant between them. The optimum interlayer exchange coupling between soft and hard layers has been found through the investigation of hysteresis loops with different exchange coupling energy densities for ECC media. The optimal interlayer exchange coupling constant, $J_{ex}/(V_1+V_2)$, is found to be $9\times10^6$ erg/cm$^3$ [5.11].

### 5.2.2 Head Field Profiles

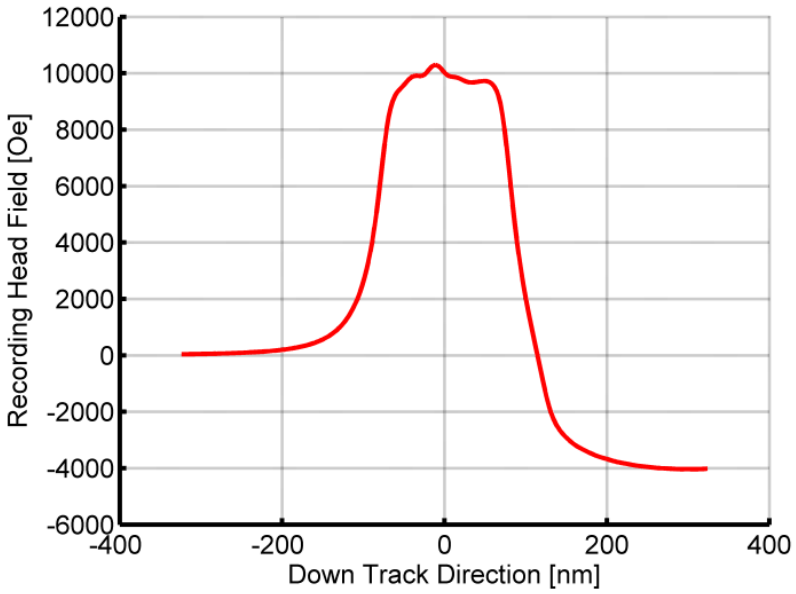


Figure 5.1: Recording head field of 75 nm wide and 150 nm length pole tip with the trailing shield of 150 nm wide and 300 nm length in down-track direction [5.11].

To compare the transition shapes of ECC media and conventional perpendicular media at 0 K and 300 K, we employ a main pole combined with a

trailing shield for the purpose of an enhanced head field gradient. Only the tip is treated micromagnetically. The main pole has a width of 75 nm and length of 150 nm. The trailing shield has a width of 150 nm and length of 300 nm. There is a 50 nm gap between main pole and trailing shield. The head flying velocity relative to the media is set at 20 m/s. The single pole tip head has an anisotropy of 10 Oe oriented in the cross track direction and magnetization of 24 kG, e.g., FeCo material. The magnetization of the trailing shield has the value of 6 kG.

### 5.2.3 Read Head

We calculated the read-back voltage using the reciprocity principle [5.6]. In order to obtain the magnetic potential distribution around the read head and recorded medium space, the three dimensional finite difference method is exploited. The shielded magnetoresistive (MR) head has shield-to-shield spacing of 30 nm, and the element width and thickness are 60 nm and 5 nm respectively [5.11].

## 5.3 Transition Jitter and Optimal Anisotropy

For high areal density, reduction of medium noise will be required. The medium noise is caused by many sources such as irregularities of media grain size, low head field gradient, thermal fluctuations, magnetic properties, etc [5.7], [5.8], [5.9]. Among them, the misplacement of transitions, which is called transition jitter, is a major cause of the medium noise. Experimentally, transition jitter can be measured by using time-domain waveform analysis. Then, zero-crossing points of the waveforms are extracted to analyze the characteristics of the received signals. Before characterizing the medium noise, we optimized the anisotropy constant of

ECC and conventional media at 0 K and at room temperature. In order to optimize the anisotropies of the two media, square-wave magnetization patterns were recorded at a linear density of 1270 kfci on AC-erased conventional media and ECC media. Approximately 100 magnetization patterns were recorded on each media, but starting each track at different positions to acquire adequate statistics. The read back voltage can be obtained from the recorded magnetization patterns using an imaginary head field generated by the read head. First of all, transition jitter is easily calculated as the standard deviation of each zero-crossing point of the read back voltage, $d_i$

$$\sigma_{jitter} = \sqrt{\frac{1}{N}\sum_{i=1}^{N}(d_i - d_m)^2} \tag{5.2}$$

where $d_m$ is averaged transition location and $N$ is the total number of transitions.

The optimum value of the anisotropy, $K_u$ of each layer is found to be $2.025\times10^6$ ergs/cm$^3$ and $6.075\times10^6$ ergs/cm$^3$ for soft and hard regions of ECC media, respectively, and $3.45\times10^6$ ergs/cm$^3$ for conventional media at 0 K [5.11]. At room temperature, the optimized anisotropy constant of conventional media was increased to $3.75\times10^6$ ergs/cm$^3$ [5.11]. The ECC media does not display a dependence of optimized media anisotropy on temperature.

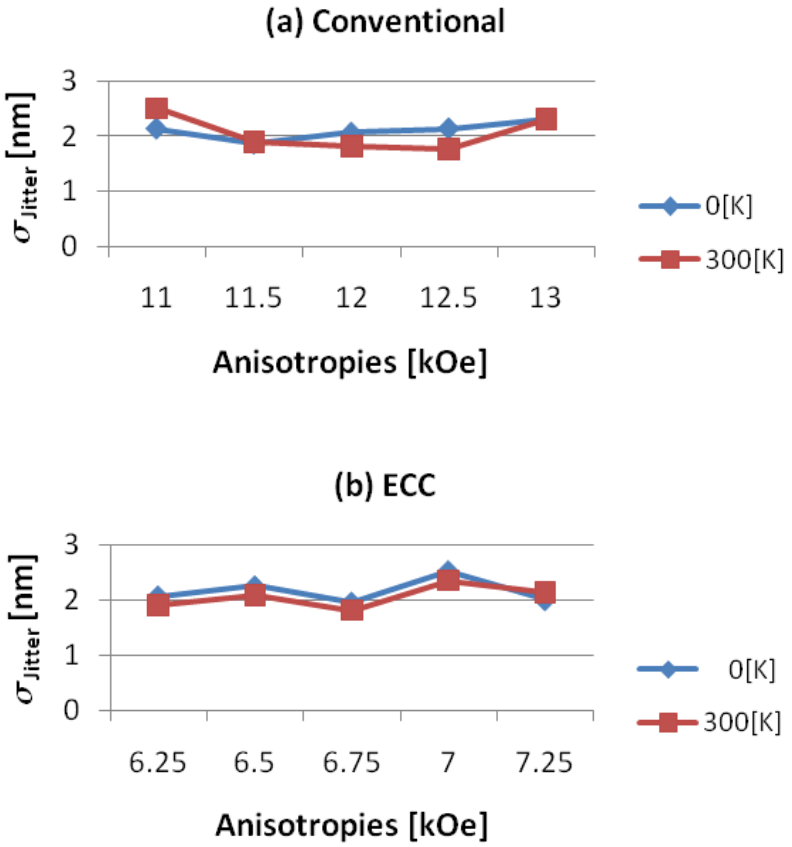


Figure 5.2: Jitter at various anisotropies for (a) conventional media and (b) ECC media at 0 K and 300 K respectively [5.11]

The jitter at optimized anisotropy shows 1.87 nm at 0 K and 1.76 nm at 300 K for conventional media and 1.96 nm at 0 K and 1.81 nm at 300 K for ECC media [5.11]. The errors bars on our jitter predictions are about 0.1 nm, implying that predicted jitter is the same for both ECC and conventional media, regardless of temperature [5.11]. Interestingly, the standard deviation of transition position (jitter) averaged across the track is smaller at 300 K than at 0 K for both types of media although the jaggedness appears to be larger at 300 K. Figure 5.3 (a), (b) and Figure 5.4 (a), (b) show sample recorded square-wave magnetization patterns with

optimized anisotropies at a linear density of 1270 kfci (a 20 nm bit length) on AC-erased conventional media and ECC media at 0 K and 300 K, respectively [5.11].

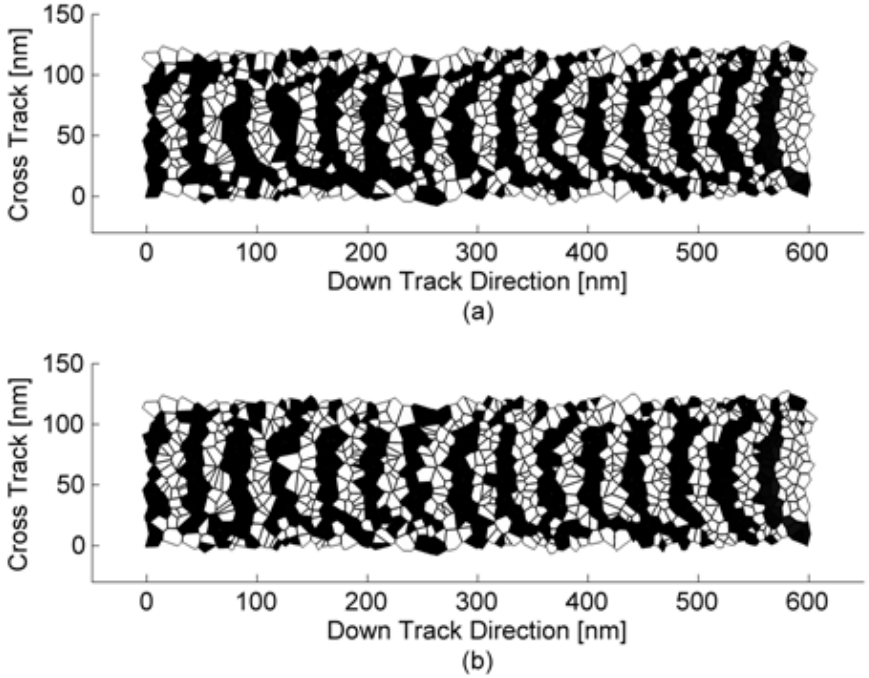


Figure 5.3: Simulated magnetization pattern with a linear density of 1270 kfci on (a) conventional media and (b) ECC media at 0 K

We also explored the jitter versus bit lengths for conventional and ECC media at 0 K and 300 K. The optimized anisotropies of each media are used in this simulation. We find the transition jitter to monotonically increase with bit length at two different temperatures for both cases [5.11]. Interestingly, ECC media has a flatter response to density at 300 K within this range of bit length. This is shown in Fig. 5.5. It may be caused by the thermal stability of the ECC media.

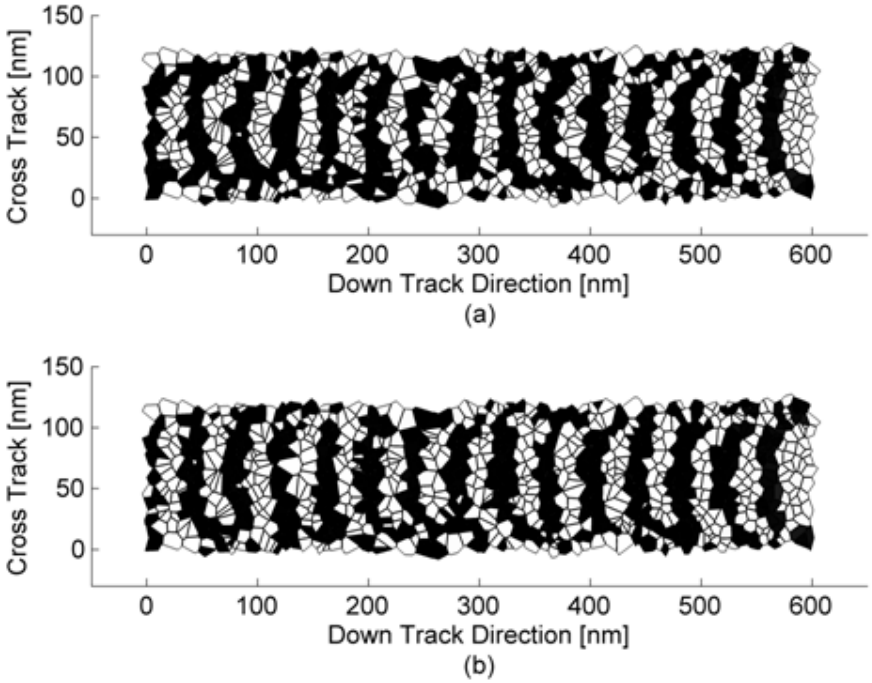


Figure 5.4: Simulated magnetization pattern with a linear density of 1270 kfci on (a) conventional media and (b) ECC media at 300 K

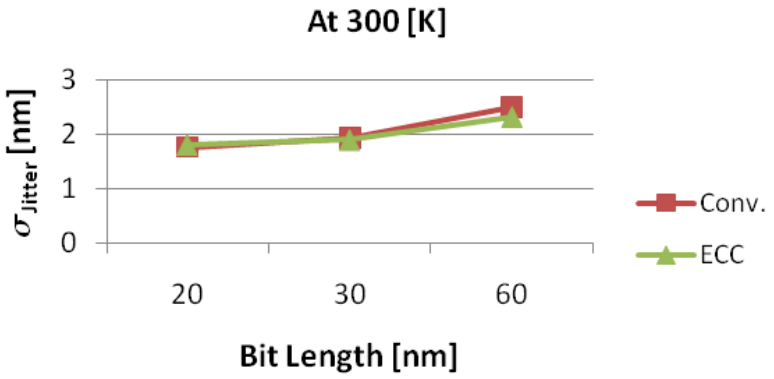


Figure 5.5: Jitter versus bit length of conventional media and ECC media at 300 K [5.11]

## 5.4 Eye Diagrams

Eye diagrams [5.10] have been used in order to analyze the transition shifts of each recording media. It provides at a glance evaluation of recording performance with amplitude and phase error of received signals. It is produced by superposing the received waveforms with an equal period. Fig. 5.6 and Fig. 5.7 show the eye diagrams of (a), conventional and (b), ECC media from the read-back signals at 0 K and 300 K respectively. For the case of conventional media with different optimized anisotropies, it shows a maximum range of 4.5 nm at 0 K and a maximum range of 4.8 nm at 300 K [5.11]. For the case of ECC media with optimized anisotropy, it shows a maximum range of 4.8 nm at 0 K and a maximum range of 4.8 nm at 300 K [5.11]. The same arbitrary unit was used for the amplitude of all eye diagrams.

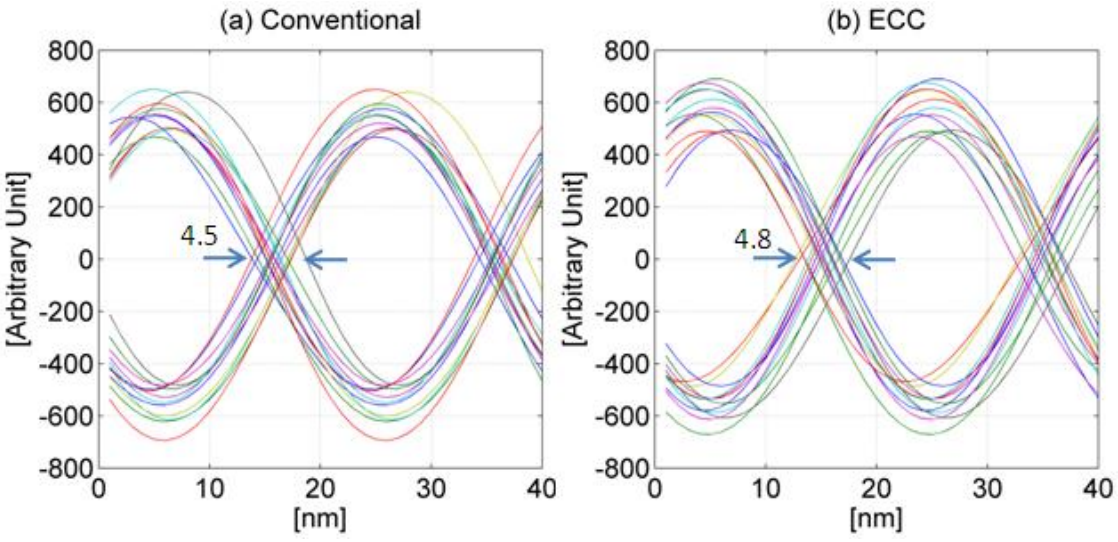


Figure 5.6: Eye diagrams with a linear density of 1270 kfci of (a) conventional media and (b) ECC media at 0 K [5.11]

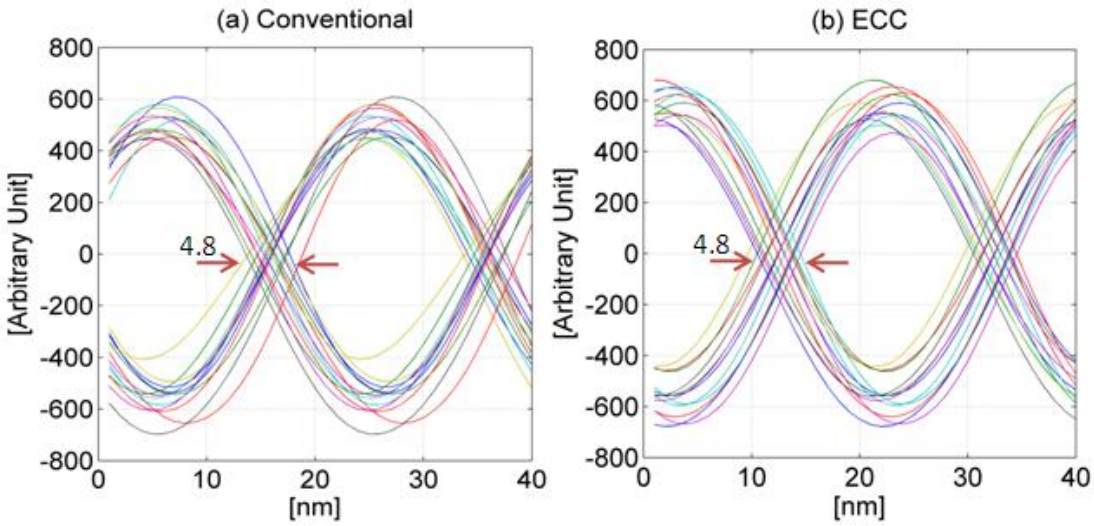


Figure 5.7: Eye diagrams with a linear density of 1270 kfci of (a) conventional media and (b) ECC media at 300 K [5.11]

The eye diagram shows that the amplitude at short bit length is higher for ECC media than conventional media by about 10 %, particularly at room temperature, despite the use of equal saturation magnetization media for each case [5.11]. Comparable plots (not shown) at low density (60 nm bit length) show identical peaks heights for the two media types. This higher amplitude at 300 K demonstrates a sharper transition recorded on the ECC media. It appears to be a consequence of a sharper head field gradient near the nucleation point combined with greater resistance to thermal fluctuations. This effect will translate into about 1dB improvement of SNR for the ECC media versus conventional media at high recording density.

## 5.5 Summary

In this study, currently feasible ECC media with moderate anisotropy ratio between soft and hard layers, and conventional media has been generated for jitter and transition shape comparisons using micromagnetic simulations. The anisotropies of the media were optimized to investigate the transition jitter characteristics of ECC and conventional media. The results show that ECC media has a flatter response to linear recording density and higher amplitude signal for short bit lengths.

# Chapter 6 Transition Noise Analysis of Recording Media

## 6.1 Introduction

A key component of perpendicular recording has long been the soft underlayer (SUL), following the original work of S. Iwasaki et al [6.1]. Typically, the SUL within a perpendicular recording system is viewed as forming a perfect image of the head that serves to double the head field. Of course, the actual physical soft underlayer has a strong exchange interaction that limits the sharpness of the image and implies that the material's permeability is strongly anisotropic [6.2], [6.3]. Usually, the special (easy) axis is chosen to lie in the cross-track direction in order to better accommodate transitions of either polarity. However, this means that the edge of the bit is written with differing effectiveness depending on whether the fringing field from the head is parallel or anti-parallel with the magnetization of the SUL. This effect will be particularly prominent in a medium having a single SUL, but should also be observable with the commonly used pair of SUL's coupled antiferromagnetically [6.4], [6.5], [6.10]. Combined with imperfect tracking and side read from the sense head, this should translate into added noise, potentially detected as jitter [6.6], [6.11].

In this chapter, transition noise characteristics of recording media with a conventional SUL and an antiferromagnetically coupled soft underlayer (AF-SUL) are predicted by micromagnetic simulation. The micromagnetic model is described

in section 2, and section 3 provides simulation results and discussions. Then, conclusions are shown in the last section.

## 6.2 Micromagnetic Model

### 6.2.1 Media Geometry

A recording system consisting of a single pole type head and trailing shield has been modeled for transition noise analysis of recording media. We generated conventional media as well as "soft" exchange coupled composite (ECC) media with moderate ratio of hard and soft anisotropy [6.6]. Both of them use a realistic grain configuration that is composed of planar Voronoi cells. Fig. 6.1 (a) shows Voronoi cell media geometry which is composed of approximately 1000 grains and non-magnetic grain boundaries of 1 nm. Therefore, the packing density of each magnetic recording media is about 80 %. These realistic grains have been mapped and discretized into a uniform three dimensional array of cubic cells ($4 \times 4 \times 4$ $nm^3$). The cubic cells are uniformly magnetized. After the mapping process, there is about a 20% discrepancy between Voronoi grains and the cubic representation in the recording layer owing to the relatively large dimension of the cubic cells. Fig. 6.1 (b) shows the Voronoi cell media geometry indexed with different colors for each grain.

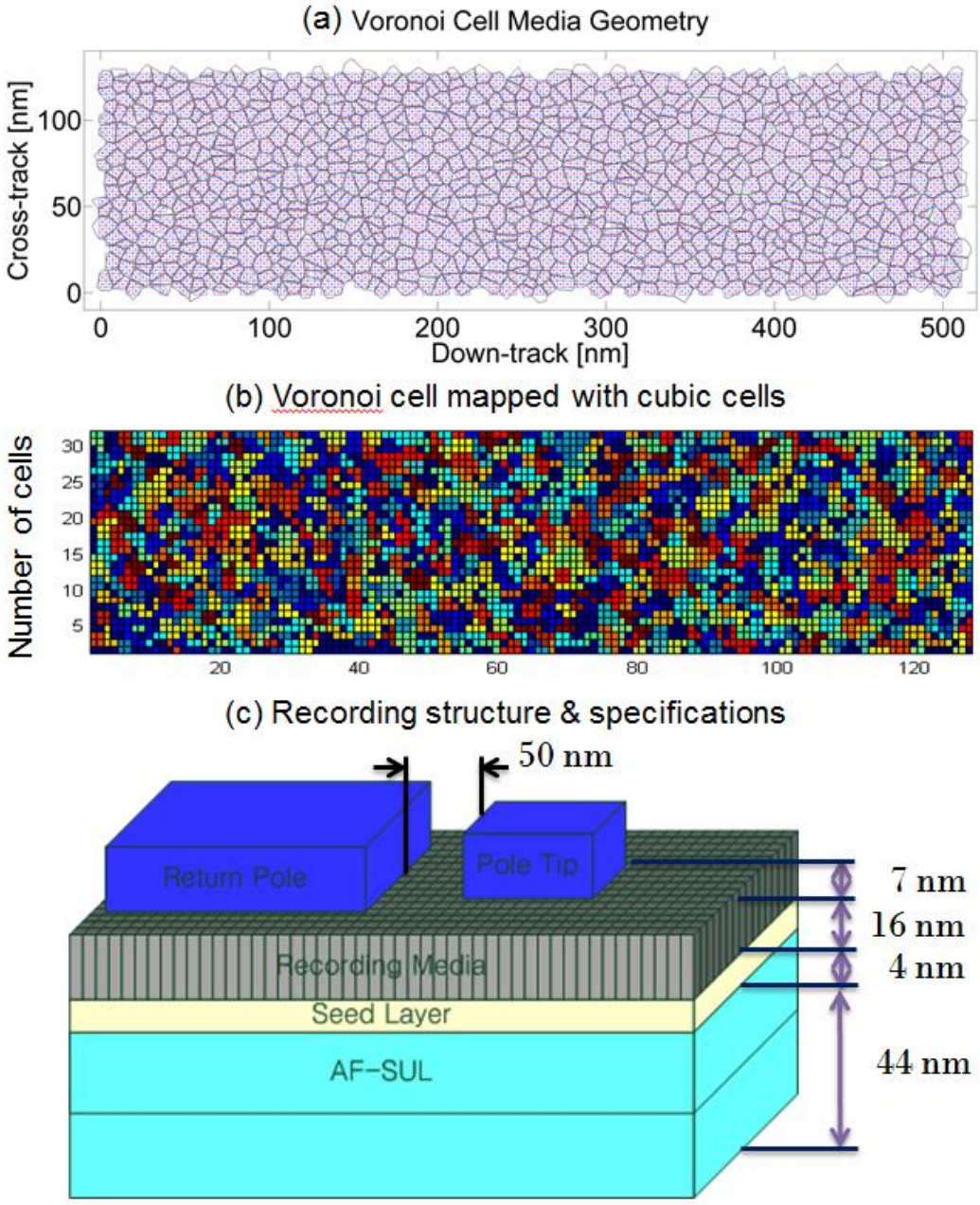


Figure 6.1: (a) Voronoi cell media geometry before discretization, (b) Voronoi cells with different colors after mapping into ($4 \times 4 \times 4$ nm$^3$) cubic cells, (c) schematic view of our perpendicular magnetic recording system, including write pole and trailing shield, with detailed parameters for each component [6.13]

Both conventional media and ECC media were taken to have a thickness of 16 nm. ECC media has a thickness of 8 nm for the top layer (magnetically soft) and a thickness of 8 nm for the bottom layer (magnetically hard), respectively. In accordance with current commercial media, a moderate anisotropy ratio of 3 between hard and soft materials has been employed. The average grain center-to-center spacing is 8.6 nm with a standard deviation of 20 %. We assumed single domain uniaxial anisotropy axes for the grains following a Gaussian distribution along the out of plane with a small standard deviation of 2°. All the saturation magnetizations of the grains, for hard ($M_{hard}$) and soft ($M_{soft}$) elements of ECC media and conventional media were set at 600 emu/cm$^3$, yielding a film magnetization of 470 emu/cm$^3$.

### 6.2.2 Magnetic Recording System

To investigate not only the transition shapes but also transition center positions of conventional perpendicular media and ECC media, a main pole combined with a trailing shield has been employed (figure 6.1 C) [6.13]. The dimensions of the main pole and the trailing shield are 40 nm × 80 nm and 80 nm × 160 nm in the cross-track and the down-track directions, respectively. There is a 50 nm gap between main pole and trailing shield. We have considered only the pole tip micromagnetically in the write head model. The main pole tip has an anisotropy of 10 Oe oriented in the cross-track direction and saturation magnetization of 24 kG. The saturation magnetization of the trailing shield has the value of 6 kG. The magnetic space between recording layer surface and the air-bearing surface was taken to be 7 nm. We find that the write head generates a peak field of 11 kOe along with peak gradients of 257 Oe/nm at the trailing edge. We considered a seed

layer of 4 nm between the recording media and the SUL. Both conventional media and ECC media are evaluated with an SUL, as well as an AF-SUL, for the transition noise analysis. The thickness of the SUL was set to 44 nm and the thickness of the AF-SUL was set to 20 nm and 24 nm for the top and bottom layers, respectively.

The inter-granular exchange coupling energy density [6.9] can be expressed as

$$\frac{\mathrm{E}_{exch}}{V} = -\mathrm{J}_{\mathrm{ex}}\left(\widehat{M_i} \cdot \widehat{M_j}\right)\frac{l_{ij}}{l_{norm}}\,, \tag{6.1}$$

where $l_{ij}$ is the boundary length between adjacent grains $i$ and $j$ and $l_{norm}$ is the average length. A typical inter-granular exchange coupling constant of 0.5 has been chosen to compensate for the excessive bit decay due to the demagnetization field. For ECC media, the optimal interlayer exchange coupling energy density between soft and hard region, $J_{ex}$ is $9\times10^6$ erg/cm$^3$ and V is the total volume of the two regions [6.6].

The magnetic recording simulation, including the recording head, recording media, and SUL has been carried out micromagnetically using a Landau-Lifshitz-Gilbert (LLG) equation. The LLG equation describes the dynamic motion for the magnetization vector of each magnetic element. The effective field combines the applied field, the uniaxial anisotropy field, the magnetostatic field and the exchange field. A 4$^{th}$-order Runge-Kutta method was used to solve the LLG equation for the time integration. In order to reduce the lengthy computational time for the magnetostatic interaction fields, the fast Fourier transform (FFT) based technique [6.7], [6.12] and graphics processing unit (GPU) computing have been used. GPU

computing uses parallel processing to accelerate the computationally intensive calculation, such as the magnetostatic tensor calculation for the media grains and the soft materials from the soft underlayer. The damping constant, α has been assumed [6.8] to be 0.2 to reduce switching times and a time step of $5\times10^{-13}$ s was employed in our simulation. For the purpose of the read-back voltage calculations, a read head combined with shields has been modeled. The shielded magnetoresistive (MR) head has shield-to-shield spacing of 30 nm, and the reader width and free layer thickness are 32 nm and 6 nm respectively.

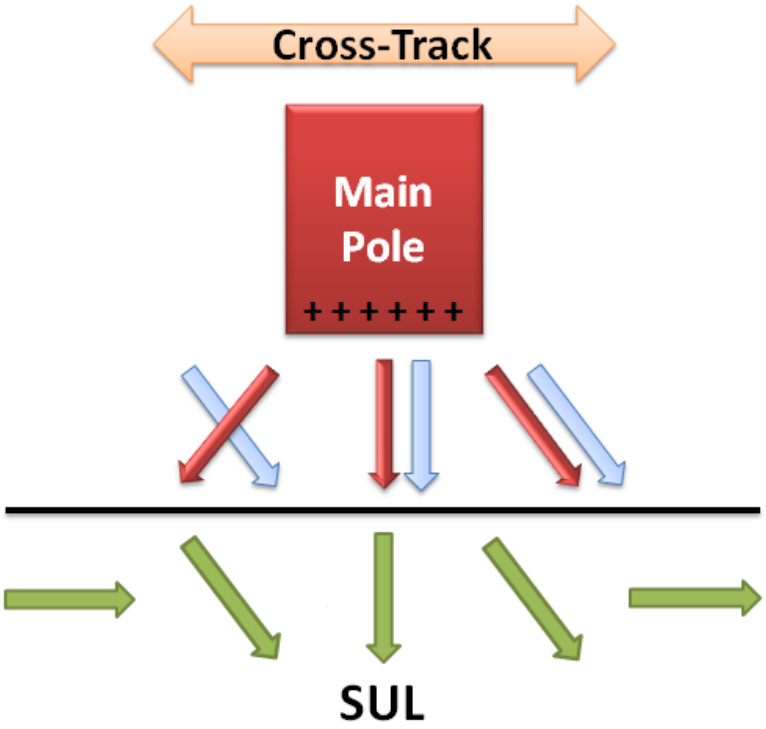


Figure 6.2: Schematic diagram of the head field from the main pole-tip (red), the induced SUL magnetization (green), and the corresponding field is generated by the SUL (blue). (The SUL easy axis is in the cross-track direction) [6.13].

## 6.3 Jitter at Various Reader Off-Centers

In perpendicular magnetic recording systems, the soft underlayer allows increased field efficiency of the write head. The SUL augments not only the writing field in the middle of the track but also the fringing field from the recording head. Unfortunately, there is a potential for noise if the SUL amplifies some parts of the head field more than others. Fig. 6.2 shows a schematic diagram of the head fields, the imaging magnetizations in the SUL, and the resulting fields from those SUL magnetizations. The easy axes of the SUL are in the cross-track direction. It can be seen that the SUL is unable to properly image the head field to the left of the main pole. This implies that the fringing field on the left side is weakened relative to that on the right side. Of course, the argument reverses when bits of the opposite polarity are written. This increased stray field may result in the erasure of the neighboring bits or lead to increased jitter if the read sensor is slightly off-track, as is common.

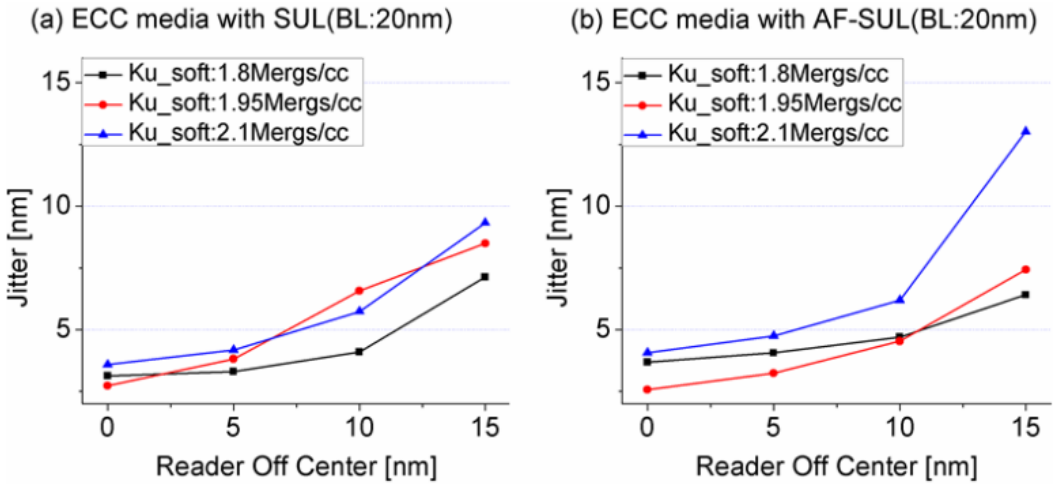

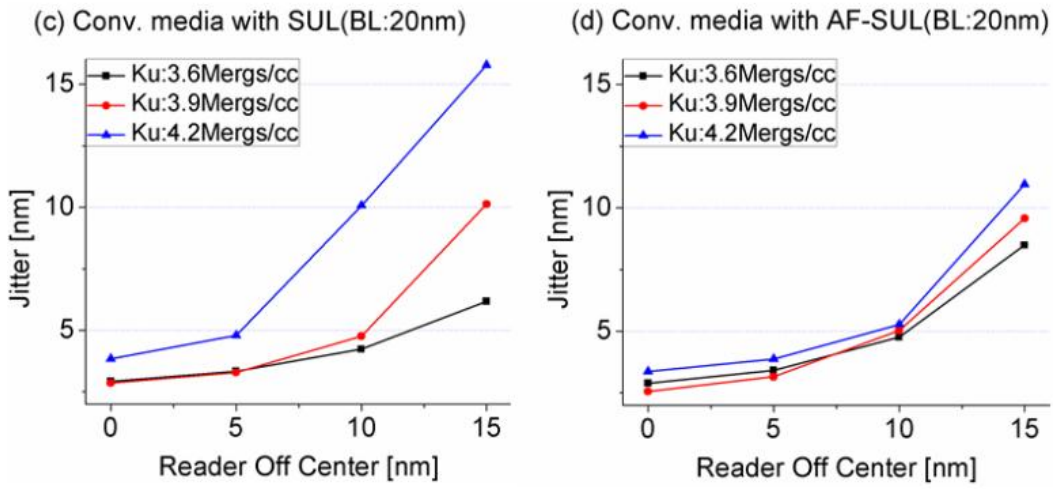


Figure 6.3: Jitter at various reader off-centers with a linear density of 1270 kfci having (a) a SUL and (b) an AF-SUL on AC-erased ECC media and (c) a SUL and (d) an AF-SUL on AC-erased conventional media respectively [6.13]

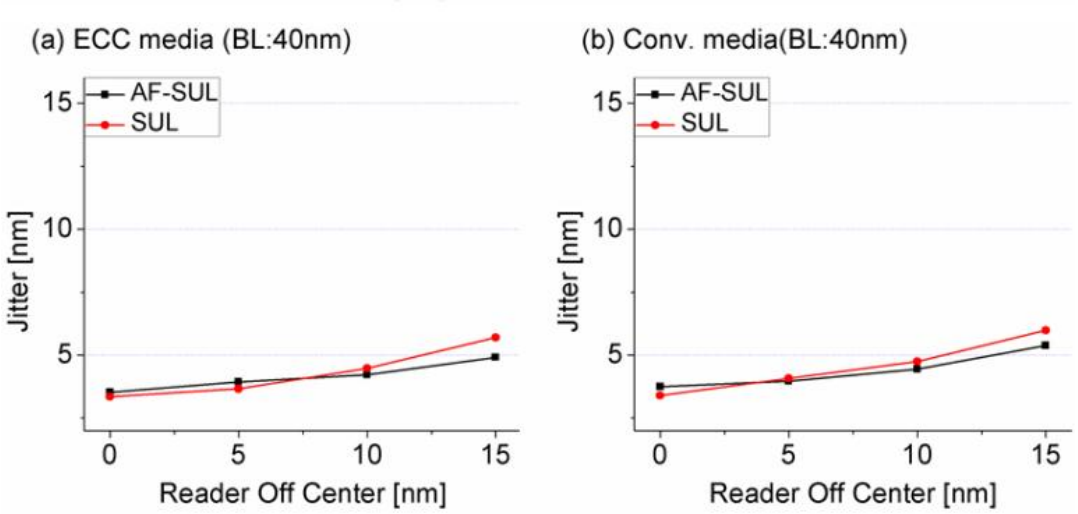


Figure 6.4: Jitter at various reader off-centers with a linear density of 635 kfci having (a) a SUL and an AF-SUL on AC-erased ECC media and (b) a SUL and an AF-SUL on AC-erased conventional media respectively [6.13]

Square-wave magnetization patterns have been recorded on AC-erased conventional media and ECC media in order to investigate the optimal anisotropies

of each media at a linear density of 1270 kfci. We calculated the read-back voltages at various different track positions from the center of the track to the left and right track edges up to 15 nm off-center for a linear density of both 1270 kfci and 635 kfci. The transition jitter, $\sigma_{jitter}$ is calculated as the standard deviation of each zero-crossing point of the read-back voltage [6.5]. In order to obtain reasonable statistics of the transition jitter, over 60 square-wave magnetization patterns have been recorded at each linear density. Fig. 6.3 (a linear density of 1270 kfci) shows the jitter (for three different values of the anisotropies of each layer) at various reader off-centers. "BL" in each figure indicates "Bit Length". From the jitter at track center, we were able to find the optimal anisotropies of each media. The optimal anisotropy of each layer is found to be $1.95\times10^6$ ergs/cm$^3$ and $5.85\times10^6$ ergs/cm$^3$ for soft and hard regions of ECC media, respectively, and $3.9\times10^6$ ergs/cm$^3$ for conventional media [6.13]. Also, fig. 6.4 (a linear density of 635 kfci) shows the jitter at various reader off-centers. These calculations used the optimum value of the anisotropy as calculated for the higher densities.

Interestingly, the jitter at reader off-centers increases less rapidly with the AF-SUL. It is most clearly seen in fig. 6.4 (linear density of 635 kfci) where the jitter with AF-SUL at the optimized anisotropy is smaller at 15 nm reader off-center for both ECC media and conventional media. The jitter at a linear density of 1270 kfci with a SUL and an AF-SUL at the optimized anisotropy for ECC media shows 2.73 nm and 2.56 nm at reader center and 8.5 nm and 7.43 nm at 15 nm reader off-center respectively [6.13]. The error bar for each case is about 13 % of the average jitter observed in each simulation, assuming uncorrelated noise [6.13]. The relative error bar, e.g., between AF-SUL and conventional SUL, is almost certainly smaller because each media sample uses the same grain structure.

Also, some of the same grains contribute to the noise regardless of whether the reader is on-track or off-center. Similarly, the jitter with a SUL and an AF-SUL at the optimized anisotropy for conventional media is 2.85 nm and 2.55 nm at reader center and 10.15 nm and 9.6 nm at 15 nm reader off-center respectively [6.13]. Incidentally, we also observe that the jitter with small anisotropy is usually lower at high reader off-centers than the jitter with optimum anisotropy: this is caused by the low anisotropy recording layer being written about 4 nm wider, i.e., 2 nm on each side, as determined by off-track signal dependence. Interestingly, the SUL writes about 1nm wider than the AF-SUL: thus, differing track widths cannot account for the SUL showing more off-track jitter.

One of the critical problems for conventional media is the high sensitivity of easy axis orientation to switching field. One consequence of this angular dependence can be seen in the results predicted for jitter as shown in fig. 6.3. For optimized anisotropy, the overall values of jitter for conventional media with both a SUL and an AF-SUL are approximately 2 nm larger than that of ECC media at 15 nm reader off-center. This is a direct consequence of ECC media only depending on the perpendicular field that is unaffected by the imaging problem of the SUL, while the conventional media is much more poorly written on one side of the track that has less transverse applied field. (The written track widths of the ECC and conventional media are identical to within 1 nm, i.e., 1/2 nm on each side. Thus, differing track width cannot account for the jitter differences.)

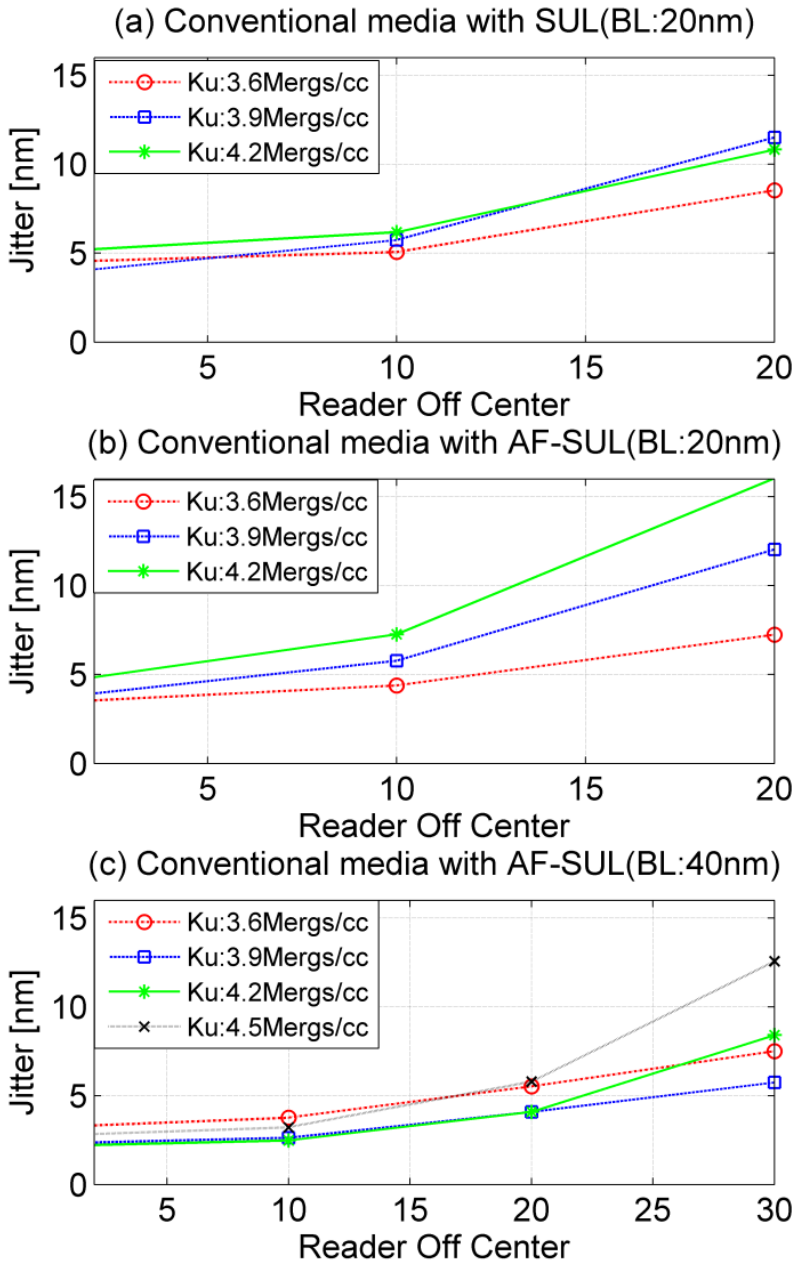


Figure 6.5: Jitter at various reader off-centers with a linear density of 1270 kfci on AC-erased recording media having (a) a SUL and (b) an AF-SUL and (c) with a linear density of 635 kfci having an AF-SUL respectively

As a check, we have also calculated the jitter for conventional media using only planar Voronoi cells without discretizing into the array of cubic cells. The optimized anisotropy field was found to be $3.6\times10^6$ ergs/cm$^3$.The simulation results shown in figure 6.5 corroborate the results using FFT based technique and GPU computing. The figure shows the jitter at various reader off-centers on AC-erased conventional media having SUL and AF-SUL with a linear density of 1270 kfci and 635 kfci. It can be seen that the jitter at the optimized anisotropy is always lower with the AF-SUL. In particular, the jitter with a SUL and an AF-SUL at 0 nm, 10 nm and 20 nm off-centers for a linear density of 1270 kfci is 3.6 nm, 5.7 nm and 11 nm and 3.3 nm, 4.4 nm and 7.2 nm respectively [6.13]. The overall values of jitter are slightly different compared to those found with the cubic discretization: this may be attributed to discretization error.

## 6.4 Transition Center Deviation

Owing to the relative ease in writing one edge compared to the other, it is expected that the bits move alternately in the cross-track direction as their polarity varies. Figure 6 shows the transition center deviation along the cross-track direction at different anisotropies on AC-erased conventional media.

A square-wave magnetization pattern indexed with the dot on each transition center is shown in figure 6.6(d). The standard deviation of the track center for cases (a), (b), and (c) (defined in figure 6.6) is calculated to be 4.01 nm, 3.37 nm and 4.93 nm, respectively [6.13]. The results suggest that transition noise is reduced for conventional media with an AF-SUL compared to that with a SUL.

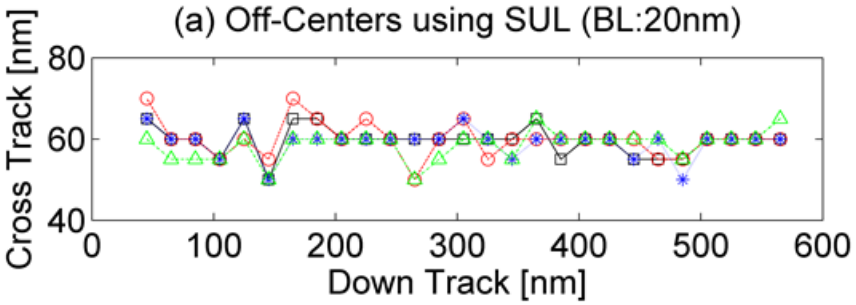
(a) Off-Centers using SUL (BL:20nm)
Cross Track [nm]
80
60
40
0
100
200
300
400
500
600
Down Track [nm]

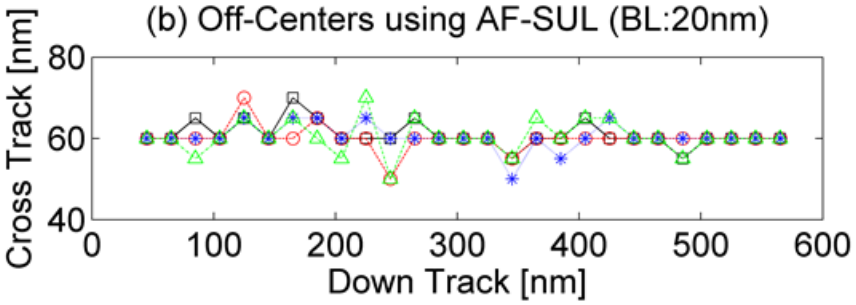
(b) Off-Centers using AF-SUL (BL:20nm)
Cross Track [nm]
80
60
40
0
100
200
300
400
500
600
Down Track [nm]

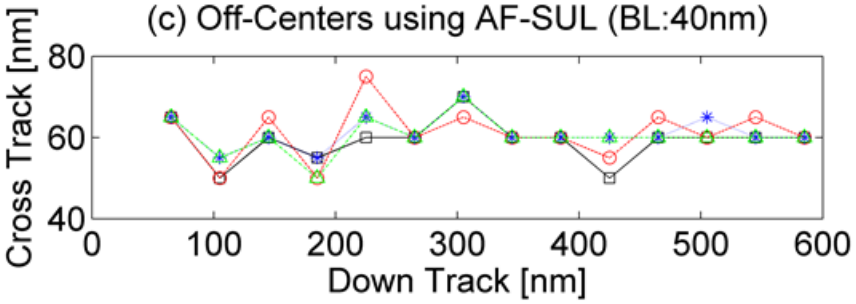
(c) Off-Centers using AF-SUL (BL:40nm)
Cross Track [nm]
80
60
40
0
100
200
300
400
500
600
Down Track [nm]

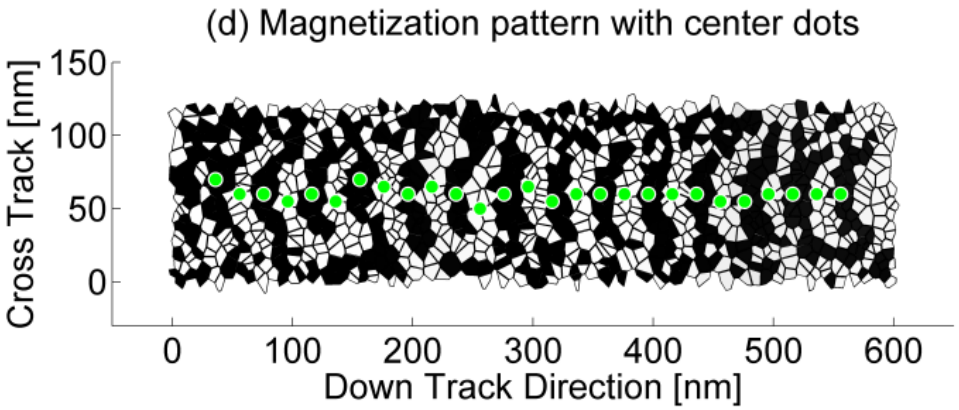
(d) Magnetization pattern with center dots
Cross Track [nm]
150
100
50
0
0
100
200
300
400
500
600
Down Track Direction [nm]

Figure 6.6: Transition center distribution along the down-track direction with a linear density of 1270 kfci on AC-erased conventional media having (a) a SUL and (b) an AF-SUL and (c) with a linear density of 635 kfci having an AF-SUL respectively. Each figure shows three separate recordings, each marked in a different color. Panel (d) shows a magnetization pattern indexed with center dots on the AC-erased conventional media having a SUL [6.13].

Figure 6.7 shows the transition center deviation with error bars at various anisotropies using the FFT based technique and GPU computing [6.13]. The transition center deviations for ECC and conventional media at a linear density of 635 kfci are calculated only at the optimized anisotropy. The standard deviation of the transition center at the optimized anisotropy for ECC media is found to be 3.44 nm with an AF-SUL and 3.77 nm with a SUL at a linear density of 1270 kfci. It is 3.81 nm with an AF-SUL and 4.31 nm with a SUL at a linear density of 635 kfci respectively. Meanwhile, the standard deviation of the transition center at the optimized anisotropy for conventional media is found to be 3.5 nm with an AF-SUL and 3.6 nm with a SUL at a linear density of 1270 kfci and 4.26 nm with an AF-SUL and 4.42 nm with a SUL at a linear density of 635 kfci respectively. According to the simulation results, the transition center deviation at the optimal anisotropy for ECC media and conventional media is always lower with the AF-SUL. We find that the transition center deviation at a linear density of 635 kfci is much higher than that at a linear density of 1270 kfci. This is probably related to the increased magnetostatic field produced by the larger previously written bits. A similar result was also observed from the standard deviation of the track center for conventional media using only planar Voronoi cells without discretizing into the array of cubic cells. We further find that the track center moves alternately with

direction of fringing field as expected from magnetostatic considerations. As can be seen in fig. 6.7 (a) and (b), the effect is minimized by an AF-SUL, but still remains detectable.

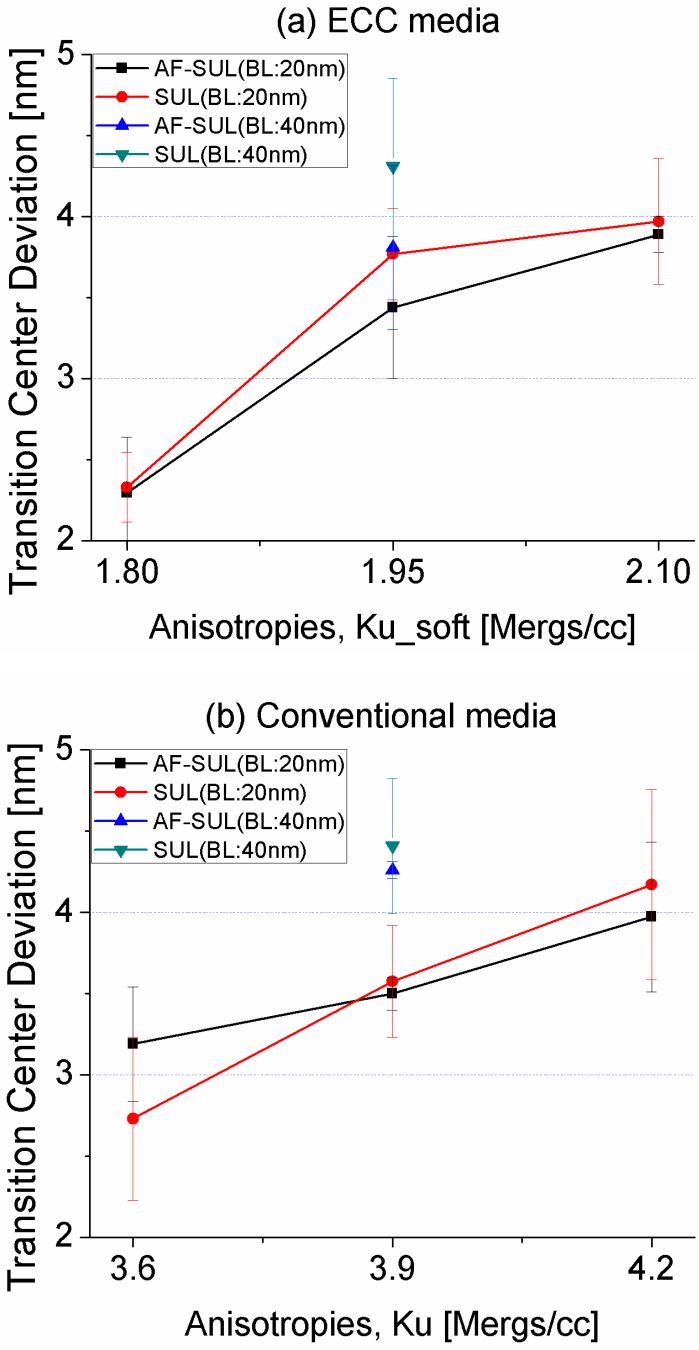

Figure 6.7: Transition center deviation at various anisotropies with a linear density of 1270 kfci and 635 kfci having a SUL and an AF-SUL (a) on AC-erased ECC media and (b) on AC-erased conventional media respectively [6.13]

## 6.5 Summary

In our study, the transition jitter of currently feasible magnetic recording systems including ECC media with moderate anisotropy ratio between soft and hard layers, and conventional media combined with SUL or AF-SUL has been computed using micromagnetics. The anisotropies of both ECC media and conventional media at a linear density of 1270 kfci have been optimized using square-wave magnetization patterns before beginning the transition noise analysis. In order to reduce the computation time for magnetostatic interaction fields, the fast Fourier transform (FFT) technique and graphics processing unit (GPU) based computing have been used. The transition noise of ECC media and conventional media was investigated using a micromagnetic SUL and AF-SUL for better accuracy compared to using a perfect imaging method. The results demonstrate that the edge of the bit is affected by whether the fringing field from the head aligns parallel or anti-parallel with the magnetization of the SUL. Therefore, both ECC media and conventional media with AF-SUL have better immunity to transition noise at the edge of the bit compared to recording media with SUL. The overall significance of this effect depends sensitively on side read and track misregistration. However, it is clear that this edge effect will become increasingly important as track widths narrow relative to the predicted cross-track deviation of 3-5 nm, and thus sampling of the edges becomes more common.

# Chapter 7

# Conclusions

In this dissertation, micromagnetic modeling using the Landau-Lifshitz formalism with Gilbert damping constant has been used to study micromagnetic processes. Fundamental magnetism and overview of magnetic recording were introduced in chapter 1. Chapter 2 introduced the stochastic LLG formalism and the definition of the energies related to magnetic nanoparticles in medical application or magnetic grains in recording system. The study of this dissertation can be categorized largely by two different magnetic applications: biomedical application (hyperthermia cancer therapy) and magnetic information storage (hard disk drive). Chapter 3 and chapter 4 mainly described magnetic processes of nanocrystalline particles for hyperthermia. Chapter 5 and chapter 6 introduced and explored the recording performance of the conventional perpendicular media and ECC media with respect to jitter, transition shape, transition center deviation, and so on.

Biocompatible particles such as magnetite and maghemite are great candidates for hyperthermia: however, their low magnetic moments may not be very attractive. Superparamagnetic $Fe_{70}Co_{30}$ particles, which have a 12 nm mean size with a narrow size distribution, were simulated micromagnetically. Predictions were made for hysteresis loops at different experimentally measured sweep frequencies. Simulation results suggested that the cubic particles had 8nm edge length, which is consistent with the experiment considering the oxide layer. The

optimized anisotropy appears to be dominated by a uniaxial term. It is suspected to come from non-uniform oxidation which introduces a shape contribution.

Dissipation mechanism of heat energy is based on Néel (hysteresis loss) and Brownian relaxation. Superparamagnetic nanoparticles subject to an oscillating field were explored with a micromagnetic model. We calculated the optimized anisotropy energy of the simulated nanocrystalline iron cobalt particles to be $3.142\times10^{-13}$ ergs which corresponds to an energy barrier of $7.6k_BT$ at room temperature. We find that application of a small field enhances the loss without the necessity for enhanced radiation. The expressions for the advantageous effects of an oscillating field as well as a static field have been derived. The calculated results suggest that the addition of a static field perpendicular to the sinusoidal oscillating applied field would be required for experimental measurement of the heating power. The frequency of magnetization attempts to surmount the energy barrier is shown to be about two orders of magnitude smaller than previously estimated. In addition, we established upper limits for the applied field magnitude, beyond which the normal linear theory will fail.

Conventional perpendicular magnetic recording also confronts the superparamagnetic limit and low write-ability despite the superior recording fields from the assistance of a soft underlayer. Currently feasible ECC media with moderate anisotropy ratio between soft and hard layers, and conventional media were generated for jitter and transition shape comparisons using micromagnetic simulations. The anisotropies of the media were optimized to investigate the transition jitter characteristics of ECC and conventional media. The results show that ECC media has a flatter response to linear recording density and higher amplitude signal for short bit lengths.

The transition jitter of currently feasible magnetic recording systems including ECC media with moderate anisotropy ratio between soft and hard layers, and conventional media combined with SUL or AF-SUL has been computed using micromagnetics. The anisotropies of both ECC media and conventional media at a linear density of 1270 kfci have been optimized using square-wave magnetization patterns before beginning the transition noise analysis. In order to reduce the computation time for magnetostatic interaction fields, the fast Fourier transform (FFT) technique and graphics processing unit (GPU) based computing have been used. The transition noise of ECC media and conventional media was investigated using a micromagnetic SUL and AF-SUL for better accuracy compared to using a perfect imaging method. The results demonstrate that the edge of the bit is affected by whether the fringing field from the head aligns parallel or anti-parallel with the magnetization of the SUL. Therefore, both ECC media and conventional media with AF-SUL have better immunity to transition noise at the edge of the bit compared to recording media with an SUL. The overall significance of this effect depends sensitively on side read and track misregistration. However, it is clear that this edge effect will become increasingly important as track widths narrow relative to the predicted cross-track deviation of 3-5 nm, and thus sampling of the edges becomes more common.

# BIBLIOGRAPHY

[1.1] Merrill, Ronald T.; Michael W. McElhinny, Phillip L. McFadden (1998). *The Magnetic Field of the Earth*. Academic Press. pp. 3. ISBN 0-12-491246-X.

[1.2] Needham, Joseph; Colin A. Ronan (1986). *The Shorter Science and Civilization in China*. UK: Cambridge Univ. Press. pp. 6, 18. ISBN 0-521-31560-3.

[1.3] Du Trémolet de Lacheisserie, Étienne; Damien Gignoux, Michel Schlenker (2005). *Magnetism: Fundamentals*. Springer. pp. 3–6. ISBN 0-387-22967-1.

[1.4] Edward Grant, "Peter Peregrinus," *Dictionary of Scientific Biography* (New York:Scribners,1975),10:532.Ron B. Thomson, "Peter Peregrinus," *Medieval Science, Technology and Medicine. An Encyclopedia*, ed. Thomas Glick et al. (New York and London: Routledge, 2005), pp. 388-389

[1.5] William Gilbert, Translated by P. Fleury Mottelay. *De Magnete*. Dover Publications Inc. 1958, 1893. p. 319-320

[1.6] B. D. Cullity, Introduction to Magnetic Materials. Addison-Wesley Publishing Company Inc., Philippines, 1972.

[1.7] Pierre Weiss, J. phys. 6, 661, 1907.

[1.8] *Quantum Theory of Magnetism: Magnetic Properties of Materials*, Robert M. White, 3rd rev. ed., Berlin: Springer-Verlag, 2007, section 2.2.7. ISBN 3-540-65116-0.

[1.9] A. Raghunathan, et al. “Theoretical model of temperature dependence of hysteresis based on mean field theory,” *IEEE Trans. on Magnetics*, vol. **46**, pp. 1507-1510, 2010.

[1.10] T. Mairoser., et al, "Influence of the substrate temperature on the Curie temperature and charge carrier density of epitaxial Gd-doped EuO films”, *Applied Physics Letters*, **98**, 102110, 2011.

[1.11] P. P. J. Haazen, et al, "Ferromagnetism in thin-film Cr-doped topological insulator $Bi_2Se_3$”, *Applied Physics Letters*, **100**, 082404, 2012.

[1.12] Ann. Phys., Paris, 3, 1948.

[1.13] IBM., "IBM 350 disk storage unit." IBM Company, Web. 14 Nov. 2011.

<http://www-3.ibm.com/ibm/history/exhibits/storage/storage_350.html>.

[1.14] Moore, Gordon., "Cramming More Components onto Integrated Circuits," *Electronics Magazine* Vol. **38**, No. 8 (April 19, 1965).

[1.15] Eli Harari, “Flash memory – The great disruptor!”, ISSCC Dig. Tech. Papers, pp. 10-15, February 2012.

[1.16] S. Iwasaki and K. Takemura, IEEE Trans. Magn., vol. **11**, 1173, 1975.

[1.17] S. Iwasaki, "Perpendicular Magnetic Recording," *IEEE Trans. on Magnetics*, vol. **16**, pp. 71-76, 1980.

[1.18] H. J. Richter, "Recent advances in the recording physics of thin-film media," *Journal of Physics D-Applied Physics*, vol. 32, pp. R147-R168, Nov 7 1999.

[1.19] G. Choe et al., “Highly in-plane oriented CoCrPtB longitudinal media for 130 $Gb/in^2$ recording”, *IEEE Trans. on Magnetics*, **39**, 633, 2003.

[1.20] Néel L, “Influence des fluctuations thermiques surl'aimantation de grains ferromagnetique tres fins”, Compt. Rend., Acad. Sci. Paris, **228**, 664-6, 1949.

[1.21] H. J. Richter, “The transition from longitudinal to perpendicular recording”, J. Phys. D: Appl. Phys. vol. **40**, pp. R149-R177, 2007.

[1.22] S. Greaves, Y. Kanai, H. Muraoka, "Trailing shield head recording in discrete track media”, *IEEE Trans. on Magnetics,* vol. **42**, no. 10, pp. 2408-2410, Oct. 2006.

[1.23] Batra S, Hannay J D, Zhou H and Goldberg J S, "Investigations of perpendicular write head design for 1 Tb/inch2", *IEEE Trans. on Magnetics,***40**, 319-325, 2004.

[1.24] Benakli M, Mallary M L, Marshall S B and Torabi A F, "Write performance of shielded pole heads on media with thin soft underlayers", J. Appl. Phys., **97**, 10P103, 2005.

[1.25] Kenchi Ito, et al., "Current progress of single-pole-type GMR heads for perpendicular recording”, *IEEE Trans. on Magnetics,* vol. **38**, no. 1, pp. 175-180, Jan. 2002.

[1.26] Francis Liu, et al., "Perpendicular recording heads for extremely high-density recording”, *IEEE Trans. on Magnetics,* vol. **39**, no. 4, pp. 1942-1948, Jul. 2003.

[1.27] M. S. Patwari and R. H. Victora, "Unshielded perpendicular recording head for 1 Tb/in$^2$”, *IEEE Trans. on Magnetics,* vol. **40**, no. 1, pp. 247-252, Jan. 2004.

[1.28] P. Wisniewski, “Giant anisotropic magnetoresistance and magneto-thermopower in cubic 3:4 uranium pnictides”, Appl. Phys. Lett., vol. **90**, 2007.

[1.29] Baibich et al., “Giant magnetoresistance of (001) Fe/(001) Cr magnetic superlattices”, *Phys. Rev. Lett*. **61**, 2472, 1988.

[1.30] B. Dieny, et al., "Giant magnetoresistance in soft ferromagnetic multilayers", Phys. Rev. B, **43**, 1297, 1991.

[1.31] Robert O'Handley, "Modern magnetic materials: principles and applications", A Wiley-Interscience Publication, 2000.

[1.32] Stuart S. P. Parkin, et al., “Giant tunneling magnetoresistance at room temperature with MgO(001) tunnel barriers, Nature Materials, vol. **3**, 862, 2004.

[1.33] S. Ikeda, et al., “Tunnel magnetoresistance of 604 % at 300 K by suppression of Ta diffusion in CoFeB/MgO/CoFeB pseudo-spin-valves annealed at high temperature”, Appl. Phys. Lett., vol. **93**, 2008.

[1.34] M. Kief, et al., "High magnetic saturation poles for advanced perpendicular writers”, *IEEE Trans. on Magnetics*, vol. **44**, no. 1, pp. 113-118, Jan. 2008.

[1.35] T. Chen and T. Yamashita, "Physical origin of limits in the performance of thin film longitudinal recording media”, *IEEE Trans. on Magnetics*, vol. **24**, 2700, 1988.

[1.36] K. E. Johnson, et al., "The effect of Cr underlayer thickness on magnetic and structural properties of CoPt”, *J. Appl. Phys.*, **67**, 4686, 1990.

[1.37] S. N. Piramanayagam, "Advanced perpendicular recording media structure with a magnetic intermediate layer”, *Applied Physics Letters*, 88, 092501, 2006.

[1.38] B. R. Acharya, et al., "Anti-parallel coupled soft underlayers for high-density perpendicular recording”, *IEEE Trans. on Magnetics*, vol. **40**, no. 1, pp. 2383, 2004.

[1.39] S. Okikawa et al., "High performance CoPrCrO single layered perpendicular media with no recording demagnetization", *IEEE Trans. on Magnetics,* vol. **36**, no. 5, pp. 2395-2395, Jan. 2000.

[1.40] T. Okikawa et al., "Microstructure and magnetic properties of CoPtCr-$SiO_2$", *IEEE Trans. on Magnetics,* vol. **38**, no. 5, pp. 1976-1978, Jan. 2002.

[1.41] Shimatsu, T., et al., "CoPtCr-$SiO_2$ perpendicular media for high density recording with a high order magnetic anisotropy energy term", *IEEE Trans. on Magnetics,* vol. **41**, no. 10, pp. 3175-3177, Oct. 2005.

[1.42] I. Kaitsu et al., "Ultra high density perpendicular magnetic recording technologies", Fujitsu Sce. Tech. J., vol. **42**, no. 1, pp. 122-130, Jan. 2006.

[2.1] Landau, L. and Lifshitz, E., "On the theory of the dispersion of magnetic permeability in ferromagnetic bodies," *Phsik. Z. Sowjetunion,* vol. **8**, pp. 153-169, 1935.

[2.2] William Fuller Brown, Micromagnetics, John Wiley & Sons, Inc. 1963.

[2.3] R. W. Chantrell, et al., "Magnetic properties and microstructure of thin film media," *J. Magn. Magn. Mater.*, **175**, pp. 137-147, 1997.

[2.4] J. Xue, R. H. Victora, "Micromagnetic calculation for superlattice magnetic recording media," *J. Appl. Phys.* 87, 6361 (2000).

[2.5] A. Aharoni, "Introduction to magnetic materials," Addison-Weley Publishing Company, Inc. 1972.

[3.1] A. Jordan, R. Scholz, P. Wust, H. Fähling and R. Felix, J. Magn. Magn. Mater. **201**, 413, 1999.

[3.2] Daniel C. F. Chan, Dmitri B. Kirpotin and Paul A. Bunn, Jr., J. Magn. Magn. Mater. **122**, 374, 1993.

[3.3] W. Andrä and H. Nowak, Magnetism in Medicine, Weinheim (Wiley-VCH, Weinheim, 2007).

[3.4] R. Hiergeist, W. Andrä, N. Buske, R. Hergt, I. Hilger, U. Richter and W. Kaiser, J.Magn. Magn. Mater, **201**, 420, 1999.

[3.5] Jean-Paul Fortin, Claire Wilhelm, Jacques Servais, Christine Menager, Jean-Claude Bacri and Florence Gazeau, J. Am. Chem. Soc. **129**, 2628, 2007.

[3.6] Robert C. O'Handley, Modern Magnetic Materials (Wiley-InterScience, New York, 2000).

[3.7] Rudolf Hergt, Wilfried Andrä, Carl G. d' Ambly, Ingrid Hilger, Werner A. Kaiser,Uwe Richter and Hans-Georg Schmidt, IEEE Trans. Magn. **34**, 3745, 1998.

[3.8] Y. H. Xu, J. M. Bai and J. P. Wang, J. Magn. Magn. Mater. **311**, 131, 2007.

[3.9] Y. H. Xu, T. Klein, Y. Jing and J. P. Wang, J. Magn. Magn. Mater. (unpublished).

[3.10] J. M. Qiu and J. P. Wang, Adv. Mater. **19**, 1703, 2007.

[3.11] J. M. Bai, Y. H. Xu and J. P. Wang, IEEE Trans. Magn. **43**, 3340, 2007.

[3.12] J. William Fuller Brown, Phys. Rev. **130**, 1677, 1963.

[3.13] J. Xue and R. H. Victora, Appl. Phys. Lett. **77**, 3432, 2000.

[3.14] Y. Jing, H. Sohn, T. Klein, R. H. Victora and J. P. Wang, J. Appl. Phys. **105**, 07B305 (2009).

[4.1] R. E. Rosensweig, J. Magn. Magn. Mater. **252**, 370 (2002).

[4.2] Hergt, R., Andra, W., d'Ambly, C.G., Hilger, I., Kaiser, W.A., Richter, U., Schmidt, H.-G., Magnetics, IEEE Trans. **34**, 3745 (1998).

[4.3] W. F. Brown, J. Appl. Phys. **30**, S130 (1959).

[4.4] R. Hergt, R. Hiergeist, I. Hilger, W. A. Kaiser, Y. Lapatnikov, S. Margel, U. Richter, J. Magn. Magn. Mater. **270**, 345 (2004).

[4.5] I. A. Brezovich, Med. Phys. Monograph **16**, 82 (1988).

[4.6] W. F. Brown, Jr., Phys. Rev. **130**, 1677 (1963).

[4.7] R. C. O'Handley, Modern Magnetic Materials, (Wiley-InterScience, New York, 2000).

[4.8] Rudolf Hergt, Silvio Dutz, J. Magn. Magn. Mater. **311**, 187-192, (2007).

[4.9] R. E. Rosensweig, "Heating magnetic fluid with alternating magnetic field," J. Magn. Magn. Mater. **252**, 370, 2002.

[4.10] H. Sohn and R. H. Victora, J. Appl. Phys. **107**, 09B312 (2010).

[4.11] Y. Jing, H. Sohn, T. Kline, R. H. Victora, and J. P. Wang, J. Appl. Phys. **105**, 07B305 (2009).

[5.1] R. H. Victora and X. Shen, "Composite media for perpendicular magnetic recording," IEEE. Trans. Magn., vol. **41**, no. 2, pp. 537-542, Feb. 2005.

[5.2] K. Tanahashi, H. Nakagawa, R. Araki, H. Kashiwase, and H. Nemoto, "Dual segregant perpendicular recording media with graded properties," IEEE. Trans. Magn., vol. **45**, no. 2, pp. 799-804, Feb. 2009.

[5.3] K. Tang, K. Takano, G. Choe, G. Wang, J. Zhang, X. Bian, and M. Mirzamaani, "A study of perpendicular magnetic recording media with an exchange control layer," IEEE. Trans. Magn., vol. **44**, no. 11, pp. 3507-3510, Nov. 2008.

[5.4] W. F. Brown, Jr., "Thermal fluctuations of a single-domain particle," Phys. Rev. vol. **130**, no. 5, pp. 1677-1686, 1963.

[5.5] J. Xue and R. H. Victora, "Micromagnetic calculation for superlattice magnetic recording media," Appl. Phys. Lett. 77, vol. **87**, no. 9, pp. 6361-6363, May 2000.

[5.6] Y. Dong and R. H. Victora, "Micromagnetic study of medium noise plateau," IEEE. Trans. Magn., vol. **45**, no. 10, pp. 3714-3717, Oct. 2009.

[5.7] M. Khan and R. H. Victora, "Micromagnetic model of perpendiculaar recording head with soft underlayer," IEEE Trans. Magn., vol. **37**, pp. 1379-1381, July 2001.

[5.8] K. Miura, H. Muraoka, and Y. Nakamura, "Effect of head field gradient on transition jitter in perpendicular magnetic recording," IEEE Trans. Magn., vol. **37**, pp. 1926-1928, July 2001.

[5.9] M. Igarashi, M. Hara, A. Nakamura, and Y. Sugita, "Micromagnetic simulation of magnetic cluster thermal activation volume, and medium noise in perpendicular recording media," IEEE Trans. Magn., vol. **39**, pp. 1897-1901, July 2003.

[5.10] P. Ziperovich, "Performance degradation of PRML channels due to nonlinear distortions," IEEE Trans. Magn., vol. **27**, pp. 4825-4827, Nov. 1991.

[5.11] H. Sohn and R. H. Victora, "Recording comparison of ECC versus conventional media," IEEE Trans. Magn., vol. **47**, pp. 4073-4076, Oct. 2011.

[6.1] S. Iwasaki and Y. Nakamura, "Analysis for the magnetization mode for high density magnetic recording," IEEE. Trans. Magn., vol. MAG-13, no. 5, pp. 1272-1277, Sep. 1977.

[6.2] Mujahid Khan and R. H. Victora, "Micromagnetic model of perpendicular recording head with soft underlayer," IEEE. Trans. Magn., vol. **37**, no. 4, pp. 1379-1381, Jul. 2001.

[6.3] Wen Jiang, Neil Smith, Mason Williams, Walter Weresin, Kenji Kuroki, Yoshihiro Ikeda, Kentaro Takano, Gautam Khera, and Roger Wood,

"Adjacent-Track Interference in Dual-Layer Perpendicular Recording," IEEE. Trans. Magn., vol. **39**, no. 4, pp. 1891-1896, Jul. 2003.

[6.4] A. Hashimoto, S. Saito, D. Y. Kim, H. Takashima, T. Ueno, and M. Takahashi, "Synthetic-antiferromagnetic coupling in subnano-crystalline FeCoB/Ru/FeCoB films," IEEE. Trans. Magn., vol. **42**, no. 10, pp. 2342-2344, Oct. 2006

[6.5] S. C. Byeon, A. Misra, and W. D. Doyle, "Synthetic antiferromagnetic soft underlayers for perpendicular recording media," IEEE. Trans. Magn., vol. **40**, no. 4, pp. 2386-2388, Jul. 2004.

[6.6] H. Sohn, R. H. Victora, "Recording comparison of ECC versus conventional media at equal grain size," IEEE. Trans. Magn., vol. **47**, no. 10, Oct. 2011

[6.7] M. Mansuripur and R. Giles, "Demagnetizing field computation for dynamic simulation of the magnetization reversal process," IEEE. Trans. Magn., vol. **24**, no. 6, pp. 2326-2328, Nov. 1988

[6.8] W. Scholz and S. Batra, "Micromagnetic modeling of head field rise time for high data-rate recording," IEEE. Trans. Magn., vol. **41**, no. 2, pp. 702-706, Feb. 2005.

[6.9] R. H. Victora, and X. Shen,"Exchange coupled composite media for perpendicular magnetic recording," IEEE. Trans. Magn., vol. **41**, no. 10, pp. 2828-2833, Oct. 2005.

[6.10] B. R. Acharya, J. N. Zhou, M. Zheng, G. Choe, E. N. Abarra, and K. E. Johnson, "Anti-parallel coupled soft under layers for high-density perpendicular recording," IEEE. Trans. Magn., vol. **40**, no. 4, pp. 2383-2385, Jul. 2004.

[6.11] M. Mallary, A. Torabi, and M. Benakli,"One terabit per square inch perpendicular recording conceptual design," IEEE. Trans. Magn., vol. **38**, no. 4, pp. 1719-1724, Jul. 2002.

[6.12] M. Patwari, S. Batra, and R. H. Victora, "Effect of pole tip anisotropy on the recording performance of a high density perpendicular head," J. Appl. Phys., vol. **93**, no. 10, pp. 6543-6545, May 2003.

[6.13] H. Sohn and R. H. Victora, "Transition noise analysis of recording media with a soft-underlayer (SUL) and an antiferromagnetic soft-underlayer (AF-SUL)," accepted by IEEE. Trans. Magn., Aug. 2012.